Modified gravity *N*-body code comparison project

Hans A. Winther,[1]⋆ Fabian Schmidt,[2] Alexandre Barreira,[3,4] Christian Arnold,[5,6]
Sownak Bose,[3] Claudio Llinares,[3,7] Marco Baldi,[8,9,10] Bridget Falck,[11]
Wojciech A. Hellwing,[3,12] Kazuya Koyama,[11] Baojiu Li,[3] David F. Mota,[7]
Ewald Puchwein,[13] Robert E. Smith[2] and Gong-Bo Zhao[11,14]

[1]*Astrophysics, University of Oxford, DWB, Keble Road, Oxford, OX1 3RH, UK*
[2]*Max-Planck-Institute for Astrophysics, D-85748 Garching, Germany*
[3]*Institute for Computational Cosmology, Department of Physics, Durham University, Durham DH1 3LE, UK*
[4]*Institute for Particle Physics Phenomenology, Department of Physics, Durham University, Durham DH1 3LE, UK*
[5]*Institute for Theoretical Physics, Heidelberg University, Philosophenweg 16, D-69120 Heidelberg, Germany*
[6]*Heidelberg Institute for Theoretical Studies, Schloss-Wolfsbrunnenweg 35, D-69118 Heidelberg, Germany*
[7]*Institute of Theoretical Astrophysics, University of Oslo, PO Box 1029 Blindern, 0315 Oslo, Norway*
[8]*Dipartimento di Fisica e Astronomia, Alma Mater Studiorum Università di Bologna, viale Berti Pichat, 6/2, I-40127 Bologna, Italy*
[9]*INAF-Osservatorio Astronomico di Bologna, via Ranzani 1, I-40127 Bologna, Italy*
[10]*INFN-Sezione di Bologna, viale Berti Pichat 6/2, I-40127 Bologna, Italy*
[11] *Institute of Cosmology & Gravitation, University of Portsmouth, Dennis Sciama Building, Portsmouth PO1 3FX, UK*
[12]*Interdisciplinary Centre for Mathematical and Computational Modeling (ICM), University of Warsaw, ul. Pawińskiego 5a, PL-02-106 Warsaw, Poland*
[13]*Institute of Astronomy and Kavli Institute for Cosmology, University of Cambridge, Madingley Road, Cambridge CB3 0HA, UK*
[14]*National Astronomy Observatories, Chinese Academy of Science, Beijing 100012, People's Republic of China*

ABSTRACT

Self-consistent *N*-body simulations of modified gravity models are a key ingredient to obtain
rigorous constraints on deviations from general relativity using large-scale structure obser-
vations. This paper provides the first detailed comparison of the results of different *N*-body
codes for the $f(R)$, Dvali–Gabadadze–Porrati and Symmetron models, starting from the same
initial conditions. We find that the fractional deviation of the matter power spectrum from Λ
cold dark matter agrees to better than 1 per cent up to $k \sim 5$–$10\,h\,\mathrm{Mpc}^{-1}$ between the different
codes. These codes are thus able to meet the stringent accuracy requirements of upcoming
observational surveys. All codes are also in good agreement in their results for the velocity
divergence power spectrum, halo abundances and halo profiles. We also test the quasi-static
limit, which is employed in most modified gravity *N*-body codes, for the Symmetron model
for which the most significant non-static effects among the models considered are expected.
We conclude that this limit is a very good approximation for all of the observables considered
here.

Key words: large-scale structure of Universe.

1 INTRODUCTION

Cosmology, and in particular observations of the large-scale struc-
ture (LSS), provide unique possibilities for testing general relativity
(GR) on length scales that cannot be probed by any other means
(see e.g. Jain & Khoury 2010; Koyama 2015; Berti et al. 2015, for
reviews). Motivated by the observed accelerating expansion of the
universe (Riess et al. 1998; Eisenstein et al. 2005; Bennett et al.
2013; Planck Collaboration XIII 2015), a number of theories have
been proposed, in which the acceleration is explained by deviations

from GR on large scales (Carroll et al. 2004; Dvali, Gabadadze &
Porrati 2000; Nicolis, Rattazzi & Trincherini 2009; Hinterbichler &
Khoury 2010), (see Clifton et al. 2012, for a comprehensive review).
In almost all cases, these theories add to the standard massless spin-
2 graviton of GR a new light scalar degree of freedom φ. Thus,
the Einstein and fluid equations of standard cosmology are aug-
mented by an equation of motion for φ. All these models are faced
with the challenge of producing sizeable effects on large scales –
the most desirable being a natural explanation of the accelerated
expansion – while at the same time passing the stringent local con-
straints on modifications to GR (Will 2014). This requires some
form of screening mechanism, that is, a way of dynamically sup-
pressing the effects of the fifth force mediated by φ in high-density

⋆E-mail: hans.a.winther@gmail.com

regions (compared to the cosmological average) where local experiments have tested GR to high precision. Such an effect is typically realized by non-linearities in the equation of motion of φ, which results in a violation of the superposition principle that suppresses the fifth force. The screening leads to a complex interplay between the large-scale distribution of matter and the magnitude of the fifth force mediated by φ.

The standard tools to compute LSS observables in the non-linear regime are *N*-body simulations. Consequently, in order to robustly test GR with cosmology, reliable *N*-body simulations of modified gravity models are a necessity. These simulations must solve the non-linear equation of φ in conjunction with the Vlasov–Poisson system that is solved in standard *N*-body simulations. The non-linear nature of the scalar field equation requires the implementation of novel numerical techniques, which is what makes *N*-body simulations of modified gravity so challenging.

To date, a number of codes have been developed to perform simulations of modified gravity. For instance, Oyaizu (2008) presented a code that simulates the Hu–Sawicki $f(R)$ model (Hu & Sawicki 2007) by solving the scalar field equation on a fixed mesh/grid (throughout we use the words mesh and grid interchangeably). Based on the work of Oyaizu (2008), Schmidt (2009b,a) developed a code (which we call DGPM here) that performed simulations of the Dvali–Gabadadze–Porrati (DGP) braneworld model (Dvali et al. 2000), also on a fixed mesh. Fixed-grid simulations of the DGP model were also performed in Chan & Scoccimarro (2009) and Khoury & Wyman (2009). More recently, efforts have been made to simulate modified gravity cosmologies on adaptively refined meshes, which allow for better resolution on small scales, where the effects of the screening are most important. These efforts resulted in the development of a modified version (Li & Zhao 2009; Zhao, Li & Koyama 2011; Li, Mota & Barrow 2011; Li & Barrow 2011) of the MLAPM code (Knebe, Green & Binney 2001), which is a serial *N*-body code. The implementation of modified gravity solvers on adaptive mesh refinement (AMR) parallelizable codes was achieved with the development of the ECOSMOG (Li et al. 2012; Li, Zhao & Koyama 2013a; Li et al. 2013b), MG-GADGET (Puchwein, Baldi & Springel 2013) and ISIS (Llinares & Mota 2013; Llinares, Mota & Winther 2014) *N*-body codes. While careful consistency checks have been performed by the authors of each code (for example, by solving test cases with known analytical solutions), no detailed comparison between codes has been performed so far. A main goal of this paper is precisely to provide a rigorous cross-check of the accuracy of the non-trivial algorithms of these codes. This is particularly important in light of the stringent accuracy requirements demanded by current and future observational campaigns.

Here, we simulate the $f(R)$, DGP and Symmetron (Hinterbichler & Khoury 2010) models with the DGPM, ECOSMOG, MG-GADGET and ISIS codes. We start all simulations of the different codes from the same initial conditions and compare their results for the matter and velocity divergence power spectra, halo mass function, as well as density, force and velocity profiles of dark matter haloes. For the case of the Symmetron model, we also measure the impact of assuming the quasi-static limit in *N*-body simulations of modified gravity, which amounts to neglecting time derivatives of φ, by comparing with the results of a version of the ISIS code that explicitly solves for the time evolution of φ.

An important consideration in such a comparison project relates to determining the target accuracy. To guide ourselves in the interpretation of the results, we use the expected accuracy of the next generation of LSS surveys. For instance, for a mission such as that to be carried out by the *Euclid* satellite[1] (Laureijs et al. 2011; Amendola et al. 2013), the non-linear matter power spectrum up to a wavenumber $k \sim 5\,h\,\mathrm{Mpc}^{-1}$ should be accurate to 1 per cent.[2] Since our goal here is to accurately calibrate modified gravity effects, we aim for an agreement in the fractional change of the matter power spectrum relative to Λ cold dark matter (ΛCDM) of 1 per cent or better. The agreement of the different codes on the absolute ΛCDM predictions is not of primary concern here, as there are dedicated comparison projects for this purpose (Schneider et al. 2015). We shall also aim for an accuracy of a few per cent in the code results for velocity statistics, the halo mass function and halo profiles.

Before proceeding, we note that the results presented in this paper contribute to recent efforts in testing and comparing *N*-body codes and codes that extract observables from simulations. For instance, there have been detailed comparisons of standard GR *N*-body codes (Scannapieco et al. 2012; Schneider et al. 2015) and also of codes that identify dark matter haloes (Knebe et al. 2011), voids (Colberg et al. 2008), halo substructure (Onions et al. 2012, 2013; Pujol et al. 2014; Hoffmann et al. 2014), galaxies (Knebe et al. 2013a), tidal debris (Elahi et al. 2013), merger trees (Srisawat et al. 2013), halo mock generation (Chuang et al. 2015) and galaxy mass reconstruction (Old et al. 2014), just to mention a few. See Knebe et al. (2013b) for a review on the current status of structure finding in *N*-body simulations. Comparison projects of these (often complex) numerical techniques are crucial to identify any worrying systematics in the theoretical predictions.

The rest of the paper is organized as follows. In Section 2, we briefly introduce and review the $f(R)$, DGP and Symmetron models that are used in our numerical comparison. In Section 3, we outline the general numerical techniques that are used to solve the modified gravity equations in a *N*-body solver. In Section 4, we summarize the main features of each of the codes and specific details in how they tackle the equations of the different models. In Section 5, we present our comparison results for the matter power spectrum (Section 5.2), the velocity divergence spectrum (Section 5.3), the halo mass function (Section 5.4), and the density, force and velocity profiles of haloes (Section 5.5). We summarize our findings and draw our conclusions in Section 6.

2 MODIFIED GRAVITY THEORY

Alternative models to ΛCDM (like the modified gravity theories studied here) are numerous (see e.g. Amendola & Tsujikawa 2010; Clifton et al. 2012; Koyama 2015), as are the problems with which they must struggle. Some models are plagued by theoretical instabilities and others require at least some degree of fine-tuning of the model parameters in order to meet observational constraints. One particularly simple extension of GR is the inclusion of a single scalar field φ to the standard GR Einstein–Hilbert action. However, when coupled to matter, the scalar field gives rise to an additional gravitational interaction, which is often referred to as a *fifth force* (see e.g. Mota & Shaw 2006; Hellwing & Juszkiewicz 2009; Amendola et al. 2013; Hellwing et al. 2013a). This fifth force can be quantified by $\gamma \equiv |\boldsymbol{F}_{\mathrm{Fifth}}|/|\boldsymbol{F}_{\mathrm{N}}|$ where $\boldsymbol{F}_{\mathrm{N}}$ is the standard Newtonian gravitational force that we obtain in the weak-field limit of GR. Several experiments (see e.g. Adelberger 2002; Bertotti, Iess & Tortora 2003; Williams, Turyshev & Boggs 2004; Will 2014) have

---

[1] http://www.euclid-ec.org/

[2] See for example Kitching & Taylor (2011) for requirements on the error envelope around the non-linear $P(k)$ for cosmic shear tomography.

constrained $\gamma \ll 1$ on Earth and in the Solar system. This seems to leave us with two possible explanations: either the fifth force is zero on all scales, i.e. $\gamma = 0$, or γ is not a constant but instead varies in space and/or time.

Models where γ is space dependent are dubbed *screened modified gravity models*, as one typically desires the fifth force to be screened in high-density environments (like the Solar system). Next, we follow Joyce et al. (2015) in the classification of the different types of screening mechanisms. A general Lagrangian density for the scalar field can be written schematically as

$$\mathcal{L} = -\frac{1}{2} Z^{\mu\nu}(\varphi, \partial\varphi, \partial^2\varphi)\partial_\mu\varphi\partial_\nu\varphi - V(\varphi) + \beta(\varphi)T_\mu^\mu, \quad (1)$$

where $Z^{\mu\nu}$ represents derivative self-interactions of the scalar field, $V(\varphi)$ is a potential, $\beta(\varphi)$ is a coupling function and T_μ^μ is the trace of the matter energy-momentum tensor. For non-relativistic matter fields, $T_\mu^\mu = -\rho_m$, the dynamics of φ therefore depend on the local density of the system, ρ_m. Around the background $\bar{\varphi}$, the dynamics of the fluctuations of φ are determined by three parameters: the mass $m(\varphi)$ (roughly given by the curvature of the effective potential), the coupling $\beta(\varphi)$ and the kinetic function $Z^{\mu\nu}(\varphi)$. Screening can be realized mainly in three different ways utilizing these three parameters:

(i) *Large mass*. If the mass of the fluctuations $m^2(\varphi)$ is large in dense environments, then the scalar field cannot propagate beyond its Compton wavelength $m(\varphi)^{-1}$ and the fifth force mediated by the scalar field is suppressed. On the other hand, in low-density environments such as the cosmological background, the mass can be light and the scalar field mediates a sizeable fifth force. This idea characterizes the so-called *Chameleon* type of screening (Khoury & Weltman 2004b,a).

(ii) *Large kinetic term*. If the kinetic function $Z^{\mu\nu}(\varphi)$ is large in dense environments, the coupling to matter is suppressed. One can either make the first or the second derivative of the scalar field large in dense environments. The former case is realized in the k-mouflage (Babichev, Deffayet & Ziour 2009; Brax & Valageas 2014) and D-BIonic type of screening (Burrage & Khoury 2014), while the latter case characterizes the Vainshtein screening mechanism (Vainshtein 1972).

(iii) *Small coupling*. If the coupling to matter $\beta(\varphi)$ is small in the region of high density, the strength of the fifth force $\boldsymbol{F}_{\text{Fifth}}$ is weak and the modifications to gravity are suppressed. On the other hand, in low-density environments, the size of the fifth force can be of the same order as standard gravity ($\gamma \sim 1$). This idea is realized in the dilaton (Brax et al. 2010) and Symmetron mechanisms (Hinterbichler & Khoury 2010).

In this code comparison project, we take $f(R)$, DGP and Symmetron gravity as our working example models that screen the fifth force via large mass, large kinetic terms and small coupling strengths, respectively. Thus, while we do not consider every individual modified gravity model proposed in the literature, our simulations do cover all classes of models. Throughout, we work with the perturbed Friedmann–Robertson–Walker space–time metric in the Newtonian gauge

$$ds^2 = -(1 + 2\Phi)dt^2 + a^2(1 - 2\Psi)\delta_{ij}dx^i dx^j, \quad (2)$$

where Ψ and Φ represent the two gravitational potentials. The dynamics of non-relativistic matter is governed by Φ, whereas the bending of light is determined by the lensing potential $\Phi_+ = (\Phi + \Psi)/2$. The modified gravity simulations employed here assume the same weak-field and non-relativistic limit as standard GR simula-

tions, i.e. higher order terms in the dark matter velocities, as well as dynamically generated vector and tensor modes are neglected.

In addition, unless otherwise specified, we assume the *quasi-static limit* for the modified gravity field equation. This refers to neglecting the time derivatives of the perturbed fields, as in $\dot{\varphi} = \dot{\bar{\varphi}} + \dot{\delta\varphi} \approx \dot{\bar{\varphi}}$, where $\delta\varphi$ is the fluctuation of the scalar field. In this paper, we shall assess the validity of the quasi-static limit in the N-body simulations of the Symmetron model.

We now describe the specific modified gravity models considered in this paper. We will often refer back to the quasi-Newtonian potential Φ_N which is defined through the Poisson equation,

$$\nabla^2\Phi_N = 4\pi G a^2 \delta\rho_m, \quad (3)$$

where $\delta\rho_m$ is the matter density perturbation.

2.1 $f(R)$ gravity

$f(R)$ gravity is arguably the most well-studied modified gravity model in the non-linear regime of cosmological structure formation. In this model, one adds a function of the Ricci scalar R to the Einstein–Hilbert action

$$S = \int d^4x \sqrt{-g} \frac{1}{16\pi G}(R + f(R)) + S_m(g_{\mu\nu}, \psi_i), \quad (4)$$

where g is the determinant of the metric $g_{\mu\nu}$ and S_m is the action of the matter fields ψ_i. In the quasi-static and weak-field limits, the relevant equations for non-linear structure formation can be written as

$$\nabla^2\Phi = \frac{16\pi G}{3} a^2 \delta\rho_m + \frac{1}{6} a^2 \delta R, \quad (5)$$

$$\nabla^2 f_R = -\frac{a^2}{3}[\delta R + 8\pi G \delta\rho_m], \quad (6)$$

where $\delta\rho_m = \rho_m - \bar{\rho}_m$ and $\delta R = R - \bar{R}$ are the density and Ricci scalar perturbations, respectively (overbars denote background averaged quantities), and $f_R = df(R)/dR$. In this formulation, f_R plays the role of the scalar degree of freedom φ that determines the fifth force and that is solved for by the numerical codes.

We specialize to the Hu–Sawicki model (Hu & Sawicki 2007), which is characterized by

$$f(R) = -m^2 \frac{c_1(R/m^2)^n}{c_2(R/m^2)^n + 1}, \quad (7)$$

$$f_R = -\frac{c_1}{c_2^2} \frac{-n(-R/m^2)^{n-1}}{[(-R/m^2)^n + 1]^2}, \quad (8)$$

where $m^2 = H_0^2 \Omega_m$ is a mass scale (not to be confused with the mass of the scalar fluctuations relevant for the Chameleon mechanism discussed above) and c_1, c_2 and n are model parameters. Note that the field value is negative ($f_R < 0$) which is necessary to ensure a positive mass of the scalar degree of freedom and hence stability of the theory. Since

$$-\bar{R} \approx 8\pi G \bar{\rho}_m - 2\bar{f}(R) = 3m^2 \left(a^{-3} + \frac{2c_1}{3c_2}\right), \quad (9)$$

one recovers a ΛCDM expansion history by setting $c_1/c_2 = 6\Omega_\Lambda/\Omega_m$. For values $(\Omega_m, \Omega_\Lambda) = (0.269, 0.731)$ (as we consider in the simulations of this paper), then $-\bar{R} \gg m^2$ and one can write

$$f_R = -n\frac{c_1}{c_2^2}\left(\frac{m^2}{-R}\right)^{n+1}. \quad (10)$$

For the simulations of this paper, we always consider $n = 1$, and hence, the remaining free parameter is c_2. However, in previous studies it has become more common to specify the Hu–Sawicki model not in terms of c_2, but in terms of the equivalent value of $\bar{f}_R$ at the present day, $\bar{f}_{R0}$. Note that by making use of equations (9) and (10), one can eliminate δR in favour of f_R in equations (5) and (6). For completeness, we note that the modified Poisson equation, equation (5), can also be written as

$$\nabla^2 \Phi = \nabla^2 \Phi_N - \frac{1}{2} \nabla^2 f_R. \tag{11}$$

This makes it explicit that in $f(R)$ models the total gravitational force is governed by a modified gravitational potential $\Phi = \Phi_N - \frac{1}{2} f_R$.

We note that the modified gravitational equations defined above hold only for the dynamical potential of the model. The lensing potential Φ_+ in $f(R)$ models (which are equivalent to scalar–tensor theories with a conformal coupling to matter) is not affected by the extra degree of freedom (Brax et al. 2008) in the weak-field limit.

The term δR on the right-hand side of equation (5) depends non-linearly on f_R (cf. equation 10). The non-linearity is what gives rise to the Chameleon screening mechanism. The screening of the fifth force is determined by the depth of the gravitational potential Φ_N. A spherically symmetric object is screened if the *thin-shell* condition

$$|f_{R\infty} - f_{Rs}| < \frac{2}{3} |\Phi_N| \tag{12}$$

is satisfied, where $f_{R\infty}$ is the f_R field away from the object and f_{Rs} is that inside the object. In order to satisfy the Solar system constraint, the Milky Way galaxy with the potential $|\Phi_N| \sim 10^{-6}$ needs to be screened. This imposes the constraint $|f_{R0}| < 10^{-6}$, if one assumes that the Milky Way galaxy is an isolated object in the cosmological background (Hu & Sawicki 2007).

For the simulations presented in this paper, we consider models with $|\bar{f}_{R0}| = 10^{-5}$ (F5) and $|\bar{f}_{R0}| = 10^{-6}$ (F6). Although the former parameter value may already be in tension with Solar system tests, we choose to simulate this model anyway, since it gives rise to larger fifth forces and places the screening threshold for haloes at mass scales that are well resolved in the simulation.[3] Our main goal in this paper is to compare the different code predictions for the fifth force, and not so much to study the observational viability of the models.

2.2 DGP

The DGP model is an example of a braneworld model. In this model, matter is confined to live in a four-dimensional brane, embedded in a five-dimensional bulk space–time. The action is given by

$$S = \int_{\text{brane}} d^4x \sqrt{-g} \left(\frac{R}{16\pi G} \right) + \int d^5x \sqrt{-g^{(5)}} \left(\frac{R^{(5)}}{16\pi G^{(5)}} \right) + S_m(g_{\mu\nu}, \psi_i), \tag{13}$$

where $g^{(5)}$ denotes the five-dimensional metric in the bulk, with $R^{(5)}$ being the Ricci scalar for $g^{(5)}$, while g and R are the induced metric on the brane and its Ricci scalar, respectively. $G^{(5)}$ and G denote the five- and four-dimensional gravitational constants. The matter fields ψ_i are confined to the four-dimensional brane. The relative

---

[3] See fig. 6 in Gronke et al. (2015a). For $|f_{R0}| = 10^{-5}$ haloes with mass $M \gtrsim 3 \times 10^{13}$ M$_\odot$ h^{-1} are screened while the smallest haloes we can resolve have $M \sim 10^{12}$ M$_\odot$ h^{-1}.

sizes of the two gravitational strengths is a parameter of the model known as the crossover scale, r_c,

$$r_c = \frac{1}{2} \frac{G^{(5)}}{G}, \tag{14}$$

below which gravity looks four-dimensional, and above which the five-dimensional aspects become important. The cosmological solutions of this model are characterized by two branches of solutions. The *normal branch* requires a dark energy term to be added to the four-dimensional part of the action to explain the accelerated expansion of the Universe (Sahni & Shtanov 2003; Lue & Starkman 2004; Schmidt 2009a); the more appealing *self-accelerating* branch does not require a dark energy field, but it is in tension with cosmic microwave background and supernovae data (Fang et al. 2008) and is also plagued by problems associated with the propagation of ghosts (degrees of freedom whose energy is unbounded from below; Luty, Porrati & Rattazzi 2003; Nicolis & Rattazzi 2004; Koyama 2007). In this paper, we focus on the normal branch of the DGP model. The dark energy component on the brane is adjusted to precisely yield a flat ΛCDM background cosmology (Schmidt 2009a).

The modifications to the gravitational law in this model are determined by a scalar field, φ, which is associated with the bending modes of the 4D brane. The brane-bending mode influences the dynamics of particles through the dynamical potential Φ, which, assuming the same boundary conditions for Φ and φ, is given by

$$\Phi = \Phi_N + \frac{1}{2} \varphi. \tag{15}$$

The equation for φ reads, in the quasi-static and weak-field limits (Koyama & Silva 2007),

$$\nabla^2 \varphi + \frac{r_c^2}{3\beta a^2} \left[(\nabla^2 \varphi)^2 - (\nabla_i \nabla_j \varphi)^2 \right] = \frac{8\pi G a^2}{3\beta} \delta\rho_m, \tag{16}$$

where $(\nabla_i \nabla_j \varphi)^2 = (\nabla_i \nabla_j \varphi)(\nabla^i \nabla^j \varphi)$, and the function $\beta(a)$ is given by

$$\beta(a) = 1 + 2H(a) r_c \left(1 + \frac{\dot{H}(a)}{3H^2(a)} \right), \tag{17}$$

where we have assumed the normal branch of the DGP model already. The quasi-static approximation in the DGP models was tested for self-consistency in section IV C of Schmidt (2009b) and was also recently shown to be an excellent approximation in Brito et al. (2014) and Winther & Ferreira (2015b).

As in $f(R)$ gravity, the propagation of photons, determined by the lensing potential Φ_+, is not directly affected by φ.

In models like DGP it is the Vainshtein screening mechanism that provides the chance to pass Solar system tests. For simplicity, we focus on spherically symmetric configurations to illustrate how the screening works. Writing down equation (16) in spherical coordinates and integrating once as $\int r^2 dr$, one gets

$$\frac{2r_c^2}{3\beta} \left(\frac{\varphi_{,r}}{r} \right)^2 + \left(\frac{\varphi_{,r}}{r} \right) = \frac{2}{3\beta} \frac{GM(r)}{r^3}, \tag{18}$$

where $M(r)$ is the mass enclosed inside a radius r, and a comma denotes partial differentiation. The solution to the last equation is given by

$$\varphi_{,r} = \frac{4}{3\beta} \left(\frac{r}{r_V} \right)^3 \left[-1 + \sqrt{1 + \left(\frac{r_V}{r} \right)^3} \right] \frac{GM(r)}{r^2}, \tag{19}$$

where we define the distance scale

$$r_V(r) = \left(\frac{16 r_c^2 G M(r)}{9\beta^2} \right)^{1/3}, \tag{20}$$

which is known as the Vainshtein radius. This radius defines the distance from the centre of the spherical overdensity below which the spatial gradient of φ becomes suppressed (and hence the fifth force effects become negligible). Explicitly, for a top-hat density profile of radius R_{th} and mass M_{th}, if $r \gg r_V > R_{th}$, then

$$\frac{\varphi_{,r}}{2} = \frac{1}{3\beta} \frac{GM_{th}}{r^2} = \frac{1}{3\beta} \Phi_{N,r}, \tag{21}$$

i.e. the fifth force becomes a sizeable fraction of the force in GR (cf. equation 15). On the other hand, if $R_{th} < r \ll r_V$, then $\varphi_{,r} \to 0$.

In the simulations of this paper, we consider two parameter values, $r_c H_0 = 1$ and $r_c H_0 = 5$. These were chosen to roughly match the F5 and F6 models, respectively, in terms of the values of σ_8 at $z = 0$.

2.3 Symmetron

The third model that we consider is the Symmetron model (Hinterbichler & Khoury 2010, see also Pietroni 2005; Olive & Pospelov 2008), whose action is given by

$$S = \int dx^4 \sqrt{-g} \left[\frac{R}{16\pi G} - \frac{1}{2}(\partial\varphi)^2 - V(\varphi) \right] + S_m(\tilde{g}_{\mu\nu}, \psi). \tag{22}$$

The matter fields, ψ, couple to the Jordan frame metric $\tilde{g}_{\mu\nu}$ which is given by a conformal rescaling of the Einstein frame metric $g_{\mu\nu}$

$$\tilde{g}_{\mu\nu} = A^2(\varphi)g_{\mu\nu}. \tag{23}$$

In the Symmetron model, the coupling function $A(\varphi)$ is given by

$$A(\varphi) = 1 + \frac{1}{2}\left(\frac{\varphi}{M}\right)^2, \tag{24}$$

where M is a mass scale. This coupling function determines the fifth force and the total gravitational force is given by

$$\boldsymbol{F} = \nabla\left(\Phi_N + \frac{1}{2}\frac{\varphi^2}{M^2}\right) = \nabla\Phi_N + \frac{\varphi\nabla\varphi}{M^2}. \tag{25}$$

The potential is taken to be of the symmetry breaking form

$$V(\varphi) = V_0 - \frac{1}{2}\mu^2\varphi^2 + \frac{1}{4}\lambda\varphi^4. \tag{26}$$

With these choices for $A(\varphi)$ and $V(\varphi)$, the model becomes invariant under the symmetry $\varphi \to -\varphi$. The value of V_0 is determined by the condition that the model gives rise to the observed accelerated expansion of the Universe (Hinterbichler et al. 2011). The field equation for φ follows from the variation of the action, equation (22), with respect to φ and reads

$$\Box\varphi = V_{eff,\varphi}, \tag{27}$$

where, for non-relativistic matter, the effective potential is given by

$$V_{eff}(\varphi) = V_0 + \frac{1}{2}\left(\frac{\rho_m}{M^2} - \mu^2\right)\varphi^2 + \frac{1}{4}\lambda\varphi^4. \tag{28}$$

In working with the model, it is convenient to define a matter density scale for symmetry breaking, ρ_{SSB}, and its associated scale factor, a_{SSB}, where $\bar{\rho}(a_{SSB}) = \rho_{SSB}$, as

$$\rho_{SSB} \equiv \mu^2 M^2 = 3H_0^2 M_{pl}^2 \Omega_m / a_{SSB}^3. \tag{29}$$

Other useful quantities are

$$\beta_0 = \frac{\varphi_0 M_{Pl}}{M^2} \; ; \; \lambda_0 = \frac{1}{\sqrt{2}\mu} \; ; \; \varphi_0 = \frac{\mu}{\sqrt{\lambda}}, \tag{30}$$

where β_0 is the coupling strength of the unscreened fifth force, λ_0 is the Compton length (giving the range of the fifth force) and φ_0 is the symmetry breaking vacuum expectation value of φ (when $\rho_m = 0$). In the simulations of this paper, we consider $\beta_0 = 1$, $\lambda_0 = 1\,h^{-1}$ Mpc and $a_{SSB} = 0.5$ which lie on the boundary of the allowed $\{a_{SSB}, \lambda_0\}$ parameter space coming from local constraints (see the discussion below equation 32). These parameter values have been previously simulated in Davis et al. (2012), Brax et al. (2012b), Llinares et al. (2014) and Llinares & Mota (2014).

In the quasi-static limit, equation (27) becomes

$$\nabla^2\chi = \frac{a^2}{2\lambda_0^2}\left(\frac{\rho_m}{\rho_{SSB}} - 1 + \chi^2\right)\chi, \tag{31}$$

where $\chi = \varphi/\varphi_0$. The full field equation, without applying the quasi-static limit, is discussed in Section 4.2.3.

During the cosmological evolution (Brax et al. 2011b, 2012a; Hinterbichler et al. 2011; Davis et al. 2012) the field sits close to the global minimum of the effective potential at $\varphi = 0$ for $a < a_{SSB}$. For $a > a_{SSB}$, the effective potential develops two minima at $\varphi = \pm\varphi_0\sqrt{1 - a_{SSB}^3/a^3}$, to which the field at $\varphi = 0$ (now a maximum) evolves, thereby spontaneously breaking the $\varphi \to -\varphi$ symmetry. Since the field can choose different minima ($+$ or $-$ branches) in different parts of the Universe, this model therefore leads to the formation of domain walls. The properties of these domain walls have been studied beyond the quasi-static approximation (Llinares & Mota 2013; Llinares & Pogosian 2014; Pearson 2014).

Screening in the Symmetron model is very similar to that in the Chameleon/$f(R)$ cases in the sense that the condition for screening is determined by the local gravitational potential. There is however the important difference that the coupling $\beta(\varphi) = \frac{\beta_0\varphi}{\varphi_0}$, which is constant for $f(R)$ gravity, now depends on the local field value. In high-density regions, $\rho_m > \rho_{SSB}$, the field moves towards $\varphi = 0$, and since the coupling is proportional to φ, the fifth force is suppressed. In the Symmetron model, the condition for the thin-shell effect is given by

$$\left|\frac{\varphi_s - \varphi_\infty}{\varphi_0}\right| \ll \Phi_N\beta(\varphi_\infty), \tag{32}$$

where φ_∞ is the φ field far away from the object and φ_s is that inside the object. In order to satisfy Solar system bounds, we get the constraint $(\frac{\lambda_0}{h^{-1}\,Mpc})^2 a_{SSB}^{-3} \lesssim \mathcal{O}(1)$ by assuming that the Milky Way galaxy is an isolated object in the cosmological background (Brax et al. 2012a).

3 MODIFIED GRAVITY SIMULATIONS

3.1 General force calculation

Cosmological dark-matter N-body simulations for standard gravity are characterized by the following two equations. First, we have the Poisson equation (3)

$$\nabla^2\Phi_N = 4\pi Ga^2\delta\rho_m, \tag{33}$$

which determines the Newtonian potential, Φ_N, given the density fluctuations $\delta\rho_m$. Secondly, we have the geodesic equation

$$\ddot{\boldsymbol{x}} + 2H\dot{\boldsymbol{x}} = -\nabla\Phi, \tag{34}$$

which tells the particles how to move. At every time step in the simulation, one (i) computes the density field from the particle positions; (ii) uses it in the Poisson equation to solve for the potential and (iii) plugs Φ into the geodesic equation to move the particles.

Table 1. Key features of the *N*-body codes compared in this paper.

Code	DGPM	ECOSMOG	MG-GADGET	ISIS	ISIS-NONSTATIC
Code paper	Schmidt (2009b)	Li et al. (2012, 2013a)	Puchwein et al. (2013)	Llinares et al. (2014)	Llinares & Mota (2014)
Base code	Oyaizu (2008)	RAMSES	P-GADGET3	RAMSES	RAMSES
Density assignment	CIC	CIC/TSC	CIC	CIC	CIC
Force assignment	CIC	CIC/TSC	Effective mass	CIC	CIC
Adaptive refinement?	No	Yes	Yes	Yes	No
Time step	Fixed	Adaptive	Adaptive	Adaptive	Adaptive
MG solver	Multigrid	Multigrid	Multigrid	Multigrid	Leapfrog
Gravity solver	Multigrid	Multigrid	TreePM	Multigrid	Multigird
Parallelization	OPENMP	MPI	MPI	MPI	MPI
Programming language	C++	FORTRAN	C	FORTRAN	FORTRAN
Models simulated	DGP	$f(R)$/DGP	$f(R)$	$f(R)$/Symmetron	Symmetron

This process is repeated from some initial redshift, $z = z_i$, until typically $z = 0$.

As we have seen in the previous section, modified gravity models alter this picture by modifying the Poisson equation that governs the total gravitational potential (like in $f(R)$ and DGP gravity), or by adding extra terms to the right-hand side of the geodesic equation (like the term $\propto \nabla A(\varphi)$ in the Symmetron model).[4] In general, modified gravity models can also differ in the background expansion rate of the Universe. In this paper, however, we shall always consider models with the same ΛCDM background evolution.

The bulk of the computing time in modified gravity simulations is spent solving the non-linear equation that governs φ (see the previous section), which can be cast in the general form

$$L[\varphi] = S(\delta\rho_m, \varphi),\qquad(35)$$

where L is some non-linear operator that acts on φ, and S is a source term that depends on the matter density fluctuations and possibly on the scalar field. The exact functional form of L and S varies from theory to theory, but as we have discussed in the previous section, this operator should possess some degree of non-linearity to ensure the presence of screening effects. The non-linearity in the equations, however, is what makes *N*-body simulations of these models so challenging. On the other hand, equation (33) is a linear elliptic partial differential equation (PDE), which means that it can be solved with efficient fast Fourier transform (FFT) methods. This is in general not possible in modified gravity models, which typically have non-linear equations. This difficulty can be overcome by employing an FFT-relaxation method (Chan & Scoccimarro 2009), if the equations are to be solved on a regular grid. However, this method does not work on irregularly shaped refinements. The codes we compare in this study solve equation (35) via direct discretization and relaxation on such an irregular grid.

In the rest of this section, we briefly outline the relaxation algorithm, describing also the main idea behind *multigrid* acceleration methods. The latter significantly improves the efficiency of the relaxation algorithms.

3.2 Iterative methods with multigrid acceleration

With the exception of the ISIS-NONSTATIC code (see next section), all codes make use of multigrid acceleration to speed up numerical convergence of the PDEs for φ. Here, we briefly review the main

---

[4] Note that any extra term in the geodesic equation can always be absorbed into the definition of a modified gravitational potential. This essentially illustrates the equivalence between the Jordan and Einstein frames.

aspects of these techniques and refer the reader to Brandt (1977), Wesseling (1992), Trottenberg, Oosterlee & Scholler (2000) and to the code papers (cf. Table 1) for further details on their implementation.

3.2.1 Gauss–Seidel iterations

The goal is to solve a differential equation that can be written in the form of equation (35). The basic algorithm consists in discretizing the equation on a grid and using an iterative scheme to obtain improved solutions given an initial guess. All codes assume periodic boundary conditions on the domain (unrefined) grid. The codes that include grid refinements use fixed boundary conditions on the boundary of the refinements, obtained by interpolating from the next coarser refinement level.

Upon discretization, the solution to equation (35) is given by the solution of the large set of algebraic equations

$$L^l[\varphi^l] = S^l,\qquad(36)$$

where L^l and S^l are the discretized versions of the L and S operators and φ^l is the field solution we aim to determine. The index l labels the refinement level of the grid. The discretization of the equation consists in writing each of the derivatives that appear in L as a combination of the values of φ on the grid cells. For instance, the codes employed here use the three- and four-point stencils

$$\partial_x^2 \varphi_{i,j,k} = \frac{1}{h^2}\left(\varphi_{i+1,j,k} + \varphi_{i-1,j,k} - 2\varphi_{i,j,k}\right)\qquad(37)$$

$$\partial_x\partial_y\varphi_{i,j,k} = \frac{1}{4h^2}\big(\varphi_{i+1,j+1,k} - \varphi_{i+1,j-1,k} \\ - \varphi_{i-1,j+1,k} + \varphi_{i-1,j-1,k}\big),\qquad(38)$$

where $\{i, j, k\}$ labels each grid cell. The iterations can be made in two different ways. If the operator L is linear, then it is best to perform *explicit* iterations, in which one rearranges the discretized equation analytically to solve directly for φ_{ijk} in each cell (this is, for instance, how the standard RAMSES code solves the Poisson equation). For non-linear problems (as those in modified gravity), an implicit iteration scheme is more suitable. In this case, one can use the *Newton–Raphson* method to solve the equation

$$T^l[\varphi^l] = L^l[\varphi^l] - S^l = 0.\qquad(39)$$

The resulting value of φ can be written as

$$\bar\varphi^l = \varphi^l - \frac{T^l}{\partial T^l / \partial \varphi^l},\qquad(40)$$

where the barred field corresponds to the updated value. Finally, one needs to specify the way in which sweeps are made across the grid in each iteration step. The simplest sweeping strategy consists in following a lexicographic ordering, in which the calculation on the cell $\{i, j, k\}$ is followed by the calculation on the cell $\{i + 1, j, k\}$, and so on. A more widespread strategy which has better convergence and parallelization properties is the so-called two colours scheme, in which the calculation is performed alternatively in cells of the same *colour*, as in the colour scheme of a chess board. In the first half-sweep all *black* cells are updated, and the second half-sweep takes care of the remaining *white* cells. Further generalizations of this scheme exist with four or even eight colours.

The iterations proceed until a certain convergence criterion is fulfilled. There are several criteria in the literature. These typically involve computing the residual, ϵ^l, of the solution defined as

$$\epsilon^l = L^l[\varphi^l] - S^l. \tag{41}$$

The convergence criterion is then given by $\|\epsilon^l\| < \epsilon_{\text{converged}}$, where $\|.\|$ is a norm (typically L_2) that is taken over the entire grid and $\epsilon_{\text{converged}}$ is a (small) predefined constant that we use to define convergence. Exact solutions of the algebraic equation have $\epsilon^l = 0$. However, owing to truncation errors (the error inevitably introduced by discretizing a continuous equation), exact solutions of the algebraic equation are not equal to the solutions of the discretized equation. The iterations are then assumed to have converged once the residual falls below a predetermined fraction of the truncation error.

3.2.2 Multigrid acceleration

In a relaxation method such as the one described above, during the first few iterations the residual decays very efficiently. However, the convergence becomes considerably slower as one approaches the true solution. This slowdown of the convergence is attributed to the fact that the components of the residual whose Fourier wavelength modes are longer than the size of the grid cell decay much more slowly than those modes whose wavelength is comparable to the grid size. The goal of multigrid methods is to speed up the convergence of these longer wavelength modes by using a hierarchy of coarser grids. In short, when the convergence of the solution starts to slow down, one interpolates the equation on to the next coarser grid of the hierarchy and solves it there. This makes the longer wavelength modes decay faster, therefore bringing the solution closer to its true value. This *coarsening* scheme can proceed up to several coarser grids. The coarser solutions can then be interpolated back to the finer (original) level.

To be more concrete, the typical way to arrange different resolutions is to use a set of grids whose resolutions are half, one quarter and so on of the target resolution. A two-grid scheme is defined in the following way. One starts by performing a given number of iterations on the target grid l. Then, when the convergence slows down, one moves to the next coarser grid $l - 1$ and performs iterations for an equation whose solution corresponds to the error $\delta\varphi^{l-1}$ of the previous solution. In the case of a linear PDE (we will turn to the non-linear case below), the equation that must be solved on the coarser grid is

$$L^{l-1}[\delta\varphi^{l-1}] = R(\epsilon^l), \tag{42}$$

where L is now a linear operator while R is a restriction operator that is chosen according to the problem and translates information from the fine grid (the target grid) to the coarse grid. Once the coarse grid iterations are done, one corrects the fine grid solution as

$$\bar{\varphi}^l = \varphi^l + P(\delta\varphi^{l-1}), \tag{43}$$

where P is now a prolongation operator which translates information from the coarse to the fine grid. In general, one uses more than one coarse grid and these processes of going up and down in resolution are called V-cycles. After one V-cycle, if convergence is not yet achieved on the target grid, then further V-cycles are performed. All the codes analysed here use V-cycles, although other arrangements are possible such as W-cycles (in these, one can move in between coarser levels several times before returning to the target grid).

In the case of non-linear equations however, this multigrid algorithm requires some changes, as it relies on the linear superposition of solutions from different grids. In the non-linear case, instead of solving following the solution for the errors on the coarse grids, one obtains improved approximations of the solution (not the error) itself. In this case, the coarse grid iterations are made according to

$$L^{l-1}[\varphi^{l-1}] = -R(\epsilon^l(\varphi^l, S^l)) + \epsilon^{l-1}(R(\varphi^l), R(S^l)) \tag{44}$$

and the coarse grid correction of the fine grid solution is given by

$$\bar{\varphi}^l = \varphi^l + P(\varphi^{l-1} - R(\varphi^l)). \tag{45}$$

4 CODE AND ALGORITHM DESCRIPTION

In this section, we briefly introduce the different *N*-body codes compared in this paper and comment on some aspects of the numerical handling of the specific model equations. We shall keep our description simple and refer the interested reader to the code papers for the details. Some of the key features of the codes are summarized in Table 1.

4.1 Code summary

4.1.1 DGPM

The DGPM code (Schmidt 2009b,a) is a fixed-grid particle-mesh code that solves the Vainshtein-type equation of motion (16). Based on the fixed-grid $f(R)$ code presented in Oyaizu (2008), it employs a second-order leapfrog scheme with fixed step size Δa in scale factor to advance particles. Densities are interpolated on to the grid using cloud-in-cell (CIC) interpolation, which is also used to evaluate derivatives on the grid. The Poisson equation for the Newtonian potential is solved using FFT on the fixed grid. The Gauss–Seidel relaxation is then performed using the Newton–Raphson method and multigrid acceleration as described in Section 3.2. At each multigrid level, 5–10 relaxation sweeps are performed. Convergence to an rms residual of less than 10^{-10} (where typical values of φ are of the order of 10^{-5}) is usually reached within three V-cycles. The step size used for this paper is $\Delta a = 0.02$, which results in 490 steps from $z = 49$ (when all our simulations start) to $z = 0$.

4.1.2 ECOSMOG

The ECOSMOG code (Li et al. 2012) is built on top of the publicly available AMR *N*-body code RAMSES (Teyssier 2002). The code can be compiled to work with CIC (like in RAMSES) or triangular-shaped cloud (TSC) schemes for the interpolation of the density and force fields. Unless otherwise specified, the ECOSMOG results shown in this paper are for TSC. The time evolution is performed with a second-order leapfrog algorithm with adaptive time steps (set by the AMR

grid, as in RAMSES). The Gauss–Seidel relaxations of the scalar field equation are performed using the Newton–Raphson methods with multigrid acceleration on all levels of the AMR grid. For the simulations in this study, the grid was set to be refined whenever the particle number exceeded 8 inside a grid cell.

In addition to the $f(R)$ and DGP gravity results shown in this paper, the ECOSMOG code has also been used to simulate dilaton (Brax et al. 2011a), Symmetron (Davis et al. 2012; Brax et al. 2013), Cubic Galileon (Barreira et al. 2013a) and Quartic Galileon (Li et al. 2013b) gravity cosmologies, as well as a general parametrization of Chameleon theories (Brax et al. 2012b). Different versions of the code differ in the detailed way the scalar field equations are solved. The performance of the relaxation algorithm is also slightly different, although, for all these models, the residuals always reach a value of $\lesssim 10^{-3}$ times the truncation error after 5–10 V-cycles. The extensions made to RAMSES to develop ECOSMOG can also be straightforwardly coupled to the hydrodynamic modules of the base code, although to date such a project has never been undertaken. In case of the DGP model, ECOSMOG solves a different version of the scalar field equation as DGPM, which will be discussed in Section 4.2.2 below.

4.1.3 MG-GADGET

The MG-GADGET code (Puchwein et al. 2013) is an extension of the cosmological hydrodynamical TreePM+SPH simulation code P-GADGET3 which is itself based on GADGET2 (Springel 2005). It features the baryonic physics modules of P-GADGET3 as well as a modified gravity solver. In addition, MG-GADGET allows the inclusion of massive neutrinos in simulations of modified gravity (Baldi et al. 2014) by making use of the particle-based massive neutrino module (Viel, Haehnelt & Springel 2010) which is implemented in P-GADGET3.

In contrast to RAMSES, P-GADGET3 does not intrinsically possess an AMR grid. To overcome this, MG-GADGET constructs an adaptively refining grid that covers the whole simulation volume by appropriately choosing nodes from the oct-tree structure of P-GADGET3's Poisson solver. This grid is then used to solve for the scalar degree of freedom using the method described in Section 3.2, i.e. using CIC density assignment and multigrid-accelerated Gauss–Seidel relaxation on the different levels of the AMR grid.

So far the code has been used to simulate the Hu & Sawicki (2007) $f(R)$ gravity model, both in collisionless (dark matter only) and hydrodynamical simulations (Arnold, Puchwein & Springel 2014, 2015). For hydrodynamical simulations, the fluid equations are solved using the same entropy-conserving smoothed-particle hydrodynamics scheme (Springel & Hernquist 2002) as P-GADGET3.

4.1.4 ISIS

The ISIS code (Llinares et al. 2014), like ECOSMOG, is a modified version of RAMSES. To date, ISIS has been used to simulate $f(R)$ gravity (Llinares et al. 2014), the Symmetron model in both the quasi-static (Llinares et al. 2014) and non-static limits (Llinares & Mota 2014), the non-static disformal gravity model (Koivisto, Mota & Zumalacarregui 2012) in its pure disformal limit, the non-static disformally coupled Symmetron model (Hagala, Llinares & Mota 2015) and the Cubic Galileon/DGP model (Winther & Ferreira 2015a). In Hammami et al. (2015) and Hammami & Mota (2015), ISIS has also been used to study hydrodynamic effects in simulations of $f(R)$ and Symmetron models.

The static version of ISIS solves the equation of motion of the scalar field using the multigrid methods outlined in the previous section. The code uses a CIC scheme to interpolate the density from the particles to the grid, and the time steps of each particle are determined by the AMR grid (as in standard RAMSES). In our simulations of the static ISIS code, each grid cell was refined whenever the particle number contained in it exceeded 8 (as in the ECOSMOG simulations).

The non-static version of ISIS (the version that goes beyond the quasi-static limit) uses a leapfrog scheme to evolve the scalar field in time. In this case, the code includes two time steps: a coarse one for the particles, which is determined by the domain grid (the non-static version does not admit refinements) and a finer one for the time evolution of the scalar field. The total number of scalar field time steps is typically 3–4 orders of magnitude larger than the number of particle time steps.

4.2 Model algorithms

In the remainder of this section, we briefly outline the strategy employed by the different codes to solve the equations of the three modified gravity models we consider.

4.2.1 $f(R)$ simulations

The simulations of the $f(R)$ Hu–Sawicki model were performed with ECOSMOG, MG-GADGET and ISIS. All these codes discretize and relax the scalar field equation of motion, equation (6), in a similar way. Instead of solving for f_R directly, the scalar field is redefined in terms of $u \equiv \ln(f_R/\bar{f}_R(a))$ which is then numerically computed. Using the variable u has considerable advantages in terms of numerical stability as it implicitly avoids unphysical positive values of f_R when performing the Newton–Raphson iterations.

Once f_R is found, the three codes compute the total force in slightly different ways. In ECOSMOG the code uses the solution for f_R to compute the δR term on the right-hand side of equation (5). The code then determines the total potential Φ by solving the modified Poisson equation in a similar way to the standard gravity solver in RAMSES. The total (modified) force, $\nabla \Phi$, is finally interpolated from the mesh to the particle positions (like in standard RAMSES).

In MG-GADGET, the total force is also obtained by solving the modified Poisson equation, but by making use of the standard tree+particle-mesh gravity algorithm of the base code. In order to do so, the modified Poisson equation is rewritten in terms of an effective mass density: $\nabla \Phi = 4\pi G(\delta \rho + \delta \rho_{\text{eff}})$, where $\delta \rho_{\text{eff}} = \frac{1}{3}\delta \rho - \frac{1}{24\pi G}\delta R$. Adding the effective to the real mass density, the values of the scalar field can be directly used in the highly optimized and efficient TreePM gravity algorithm of P-GADGET3 to compute the total force.

Although these two methods for solving the modified Poisson equation are mathematically equivalent, they can yield different numerical accuracies. In addition to the convenience of using the standard Poisson solver, MG-GADGET's effective mass algorithm avoids an interpolation of the scalar field gradient (the fifth force) from the adaptive mesh to the particle positions, as the tree force is directly computed there. It might, nevertheless, be somewhat less accurate in highly screened regions than the method used in ECOSMOG due to numerical summation errors in the tree gravity, which can result in less precise screening of the fifth force. This causes somewhat larger random force errors for the individual particles while the integrated effects are expected to average out. Fig. 1 displays profiles of the
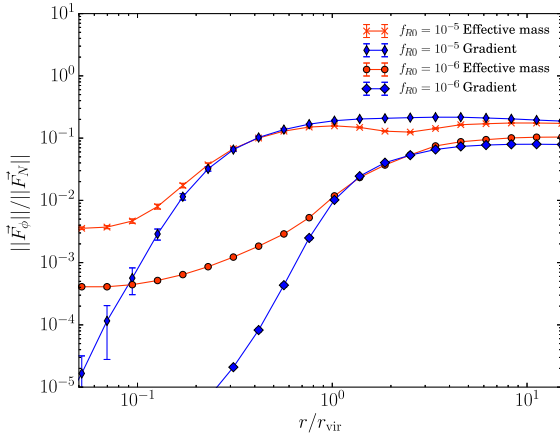
Figure 1. Fifth to Newtonian force ratio profile, F_ϕ/F_N, obtained from interpolating the scalar field gradient from the grid to the particle positions (blue) and from the effective matter density method using the tree force calculation (red) in MG-GADGET for the $f(R)$ simulations. The profiles shown are the average for haloes with masses $M \in [1 \times 10^{14}, 5 \times 10^{14}]$ M$_\odot$ h^{-1}. The error bars are the variance of this average.

ratio of fifth to Newtonian force in dark matter haloes obtained via interpolation of the gradient from the grid (blue) and via the effective density scheme (red). Although it is noticeable that there are significant differences between the two methods on small scales, this occurs only in a regime where the fifth force is already highly screened ($\lesssim 1$ per cent of normal gravity). As force errors of around one percent also occur in the standard tree gravity algorithm, these errors are expected to be negligible. In the region where screening just sets in (which several observables might be sensitive to) the curves almost perfectly match each other. Consequently, the mentioned inaccuracies in the fifth force calculation will not change the total force significantly and will therefore only have a very minor impact on observables (as we shall see in more detail in the next sections).

Finally, in ISIS, the code computes the gradient of the scalar field and interpolates it on to the particle positions. The GR gravitational potential, Φ_N, is solved exactly as in RAMSES, and the total force at the particle positions is given by $\nabla\Phi = \nabla\Phi_N - \nabla f_R/2$ (cf. equation 11).

We refer the reader to the respective code papers for more details about how ECOSMOG, MG-GADGET and ISIS solve the modified gravity equations, code tests, and explicit discretization of the equations.

4.2.2 DGP simulations

The simulations of the DGP braneworld model shown here were performed with the DGPM and ECOSMOG codes. In DGPM, the scalar field equation is discretized as it is written in equation (16). Some of the simulations using DGPM presented in Schmidt (2009b,a) employed a Gaussian smoothing of the density field in order to improve convergence. For the analysis of this paper, however, no such smoothing was performed.

In the strategy employed by the ECOSMOG code, equation (16) is manipulated analytically before being discretized. This manipulation is called the *operator-splitting trick* (Chan & Scoccimarro 2009; Li et al. 2013a,b), which we describe next. Equation (16) can be cast as

$$(1-w)\left(\nabla^2\varphi\right)^2 + \alpha\nabla^2\varphi - \Sigma = 0, \tag{46}$$

where

$$\alpha = \frac{3\beta(a)a^2}{r_c^2}, \tag{47}$$

$$\Sigma = \left(\nabla_i\nabla_j\varphi\right)^2 - w\left(\nabla^2\varphi\right)^2 + \frac{8\pi Ga^4}{r_c^2}\delta\rho, \tag{48}$$

and w is a constant numerical factor. Equation (46) can be solved once to yield

$$\nabla^2\varphi = \frac{\alpha \pm \sqrt{\alpha^2 + 4(1-w)\Sigma}}{2(1-w)}. \tag{49}$$

Decomposing the term $\nabla_i\nabla_j\varphi$ into its trace and traceless part (this is the operator-splitting trick),

$$\nabla_i\nabla_j\varphi = \frac{1}{3}\gamma_{ij}\nabla^2\varphi + \hat{\nabla}_i\hat{\nabla}_j\varphi, \tag{50}$$

it is possible to show, after a bit of algebra, that

$$\Sigma = \left(\hat{\nabla}_i\hat{\nabla}_j\varphi\right)^2 + \frac{8\pi Ga^4}{r_c^2}\delta\rho, \quad \text{if } w = \frac{1}{3}. \tag{51}$$

That is, if $w = 1/3$, then this cancels out the term $\nabla^2\varphi$ in Σ. The reason why this is useful is because, upon discretization, the traceless part $\hat{\nabla}_i\hat{\nabla}_j\varphi$ does not depend on the grid cell value, φ_{ijk}, but only on its neighbours. Hence, in the equation that ECOSMOG solves, which is equation (49), φ_{ijk} appears only on the left-hand side, and not inside the square root. This is found to improve considerably the performance of the code. Moreover, by taking out φ_{ijk} from inside the square root one also avoids potential problems associated with imaginary square roots caused by some bad initial guess for φ_{ijk}. The sign of the square root in equation (49) is chosen to be the same as the sign of the α function. This is the solution which corresponds to the physical (linear theory) result that $\nabla^2\varphi \to 0$, when $\delta\rho \to 0$.

Once φ is found on every grid cell, both DGPM and ECOSMOG compute the total force, $\nabla\Phi$, as the sum of normal gravity and the fifth force, $\nabla\Phi = \nabla\Phi_N + \nabla\varphi/2$.

For completeness, we point out that if $\delta\rho$ becomes negative (as it does in voids), then there is the risk that the argument of the square root in equation (49) may become negative. This does not happen for the DGP model, but similar Vainshtein screening models such as the Cubic (Barreira et al. 2013a) and Quartic Galileon (Li et al. 2013b; Barreira et al. 2013b) do suffer from imaginary square-root problems in low-density regions (see Winther & Ferreira (2015b) for a discussion about the meaning of these imaginary square-root problems).

4.2.3 Quasi-static and non-static simulations of the Symmetron model

The simulations of the $f(R)$ and DGP models are performed under the quasi-static approximation. To go beyond this approximation means to explicitly take into account the time-derivative terms of the scalar field in the equations. This way, the solution for the scalar field at a given time depends also on its past evolution, as opposed to depending only on the matter configuration at that given time. To date, non-static cosmological simulations of modified gravity have been performed for the Symmetron and disformal gravity models using the explicit leapfrog method (Llinares & Mota 2013, 2014; Hagala et al. 2015), for $f(R)$ gravity using the implicit Newton–Gauss–Seidel method (Bose, Hellwing & Li 2015) and for the DGP and the Cubic Galileon models using both of the methods mentioned

above, but only in a spherical symmetric space–time (Winther & Ferreira 2015b).

For the Symmetron model, the full Klein–Gordon equation (27) reads

$$\ddot{\chi} + 3H\dot{\chi} - \frac{\nabla^2 \chi}{a^2} = -\frac{1}{2\lambda_0^2}\left[\frac{a_{\rm SSB}^3}{a^3}\chi\eta - \chi + \chi^3\right], \qquad (52)$$

where η is the matter density in units of the background value. In ISIS-NONSTATIC (the modified version of ISIS that relaxes the quasi-static approximation), the second-order equation of motion of the scalar field is decomposed into a system of two first-order equations as

$$\dot{\chi} = \frac{q}{a^3}, \qquad (53)$$

$$\dot{q} = a\nabla^2\chi - \frac{a^3}{2\lambda_0^2}\left[\frac{a_{\rm SSB}^3}{a^3}\chi\eta - \chi + \chi^3\right], \qquad (54)$$

which are used to propagate both χ and q using a leapfrog algorithm. The 'position' χ and 'velocity' q are displaced from each other by 1/2 time step and the discretized equations become

$$\chi_n = \chi_{n-1} + \dot{\chi}_{n-1/2}\Delta t, \qquad (55)$$

$$q_{n+1/2} = q_{n-1/2} + \dot{q}_n\Delta t, \qquad (56)$$

where $f_n \equiv f(t_n)$. The spatial derivatives of χ in the formulae above are calculated from the grid using a five-point stencil, see Llinares & Mota (2014) for a detailed description of the implementation of the scheme.

The quasi-static simulations of the Symmetron model are performed by discretizing equation (52) and neglecting the first two terms on the left-hand side. In this case, one does not need to explicitly evolve the scalar field. Instead, given the matter distribution, η, at a given time step, the code relaxes the equation that contains only the scalar field and its second spatial derivative (not time derivatives), using the multigrid methods described in Section 3.2.

5 RESULTS

In this section, we present the main results of this code comparison project. We present and discuss the different code results for the matter and velocity divergence power spectra and halo mass function, as well as the halo profiles of the scalar degree of freedom, forces and density.

5.1 Simulation setup

All the simulations performed in this study have used the same initial conditions, which were generated using 2LPT (Crocce, Pueblas & Scoccimarro 2006) from a ΛCDM cosmology with $\Omega_{\rm m} = 0.269$, $\Omega_\Lambda = 0.731$, $h = 0.704$, $n_{\rm s} = 0.966$ and $\sigma_8 = 0.8$. The simulations have $N = 512^3$ particles in a box of size $B = 250\,h^{-1}$ Mpc and they start at redshift $z = 49$. All modified gravity models simulated here have the same expansion history as a ΛCDM model with the above parameters and the evolution of density perturbations at high redshifts ($z \gtrsim 10$) is almost identical to that of the ΛCDM model justifying the use of the same initial conditions.

For simulations with a RAMSES-based code, we used a coarse-level grid with refinement level $l_{\rm min} = 9$ corresponding to 512^3 coarse cells. Each cell was refined if the number of particles contained in it exceeded 8. The maximum level of refinement corresponded to

$l_{\rm max} = 15$ for F6 and $r_{\rm c}H_0 = 5$ and $l_{\rm max} = 16$ for F5 and $r_{\rm c}H_0 = 1$. For the MG-GADGET simulations, the relative tree opening criterion was used where the tree is open when the relative force acceleration error is larger than 0.0025, the force softening was 18.75 kpc h^{-1} and for the long-ranged forces a particle-mesh grid with 512^3 grid cells was used. The force softening corresponds to the grid spacing at level $\simeq 14$ in the AMR hierarchy.

The codes compared in this project differ in two aspects: (i) the exact way in which the equations of the scalar field are solved and (ii) the force calculation and time stepping, which were taken from the original codes they were built from (e.g. P-GADGET3 and RAMSES). To separate the differences that arise from these two aspects, simulations of the standard ΛCDM model were also performed. This way, differences between the code predictions for the absolute value of a measured quantity (e.g. P_k) are affected by both aspects. On the other hand, comparisons of the code predictions for the relative difference to ΛCDM (e.g. $\Delta P_k/P_{k,\Lambda{\rm CDM}}$) should be mostly determined by aspect (i) and not so much by aspect (ii).

The run-time of the modified gravity simulations we have performed was about 5–10 times that of the corresponding ΛCDM simulation.

5.2 Matter power spectrum

As a consistency check, we have measured the matter power spectrum, P_k, from the simulations using three independent codes. One is the POWMES code (Colombi et al. 2009), which uses Fourier transforms with folding methods to compute P_k. Another is a code written by one of the authors of this paper (RS), which works similarly to POWMES except that it does not apply folding methods. Both these codes deconvolve the window function of the density assignment and shot-noise is subtracted. Lastly, we have also measured the power spectrum using a density field obtained with the *Delaunay Tesselation Field Estimator* (DTFE) method of Schaap & van de Weygaert (2000). We have found that the results from these three codes agree very well (to the 1 per cent level[5]) and when considering $\frac{\Delta P}{P_{\rm LCDM}}$ the agreement was below 0.1–0.5 per cent for all scales of interest. All the plots shown in this paper are those obtained using the code made by RS mentioned above. We show the power spectrum out to the particle Nyquist frequency, $k_{\rm max} = \pi N_{\rm particles}^{1/3} B_0^{-1} = 6.4\,h\,{\rm Mpc}^{-1}$, of the simulations.

Next, we present our results for the matter power spectrum, discussing separately the results obtained for ΛCDM, $f(R)$, DGP and Symmetron models.

5.2.1 ΛCDM

Before comparing the results for the modified gravity models, it is instructive to have a look at how the codes compare for ΛCDM. This is shown in the left-hand panel of Fig. 2 for $z = 0$ (solid) and $z = 1$ (dashed). The red and green lines show, respectively, the ratio of the ISIS and ECOSMOG result to that of MG-GADGET. One notes that the two RAMSES-based codes predict less power (4–5 per cent at $z = 0$, $k \approx 7\,h\,{\rm Mpc}^{-1}$) than the MG-GADGET simulations. This can be attributed to the different ways the base codes compute the gravitational force on small scales. In P-GADGET3, the force on

---

[5] For this comparison, we have ignored the four largest Fourier modes where cosmic variance is significant since the different codes use different methods to estimate the power on these scales which can lead to quite large differences.
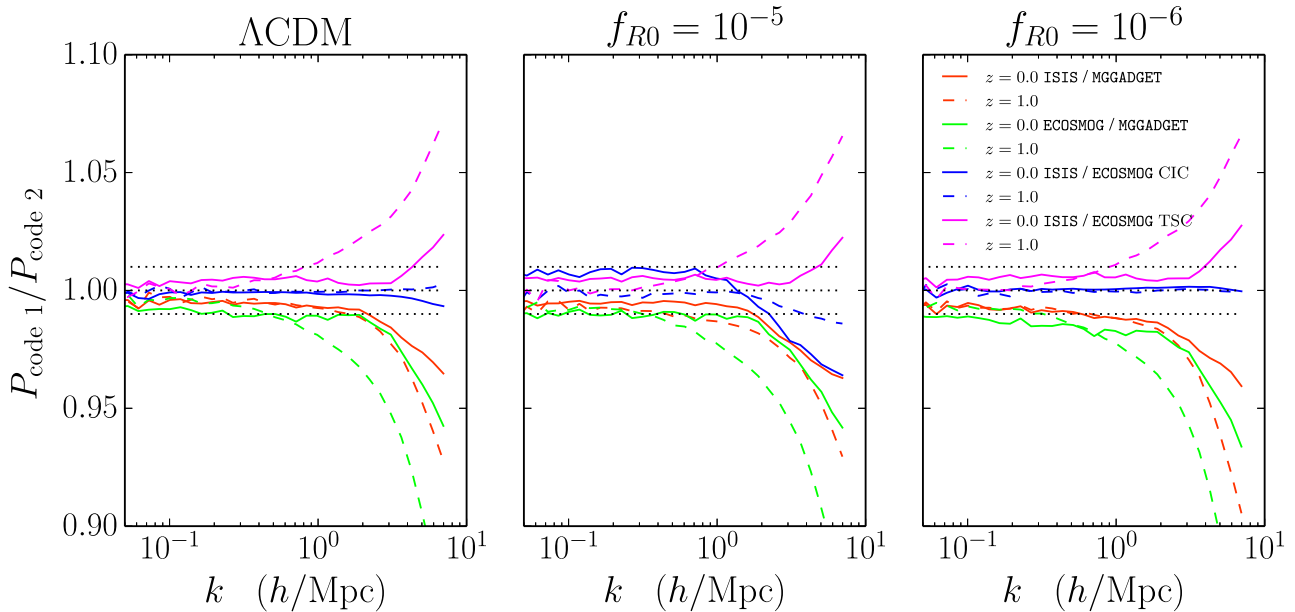
Figure 2. Comparison of the matter power-spectrum results of the ECOSMOG, MG-GADGET and ISIS codes for the ΛCDM (left), F5 (middle) and F6 (right) models, as labelled. When comparing the two RAMSES-based codes (ISIS and ECOSMOG), we show the ECOSMOG results from simulations run with CIC and with TSC interpolation schemes, as labelled.

large scales is computed using a particle-mesh method, just like in RAMSES. On small scales, however, P-GADGET3 switches to a tree method, whereas in RAMSES the calculation remains as on large scales. The accuracy of the RAMSES code on small scales depends also on the criteria to trigger a refinement of the AMR grid. In all RAMSES-based AMR simulations of this paper, the grid refines itself whenever the particle number inside a given cell exceeds 8. Due to these differences between the force calculation on small scales, one should therefore not expect perfect agreement between the RAMSES-based and GADGET-based codes. We refer the reader to Schneider et al. (2015) for a more detailed comparison study of the performance of the RAMSES, GADGET and also PKDGRAV3 codes in ΛCDM simulations.

The result shown by the blue and pink lines illustrates the impact of using different schemes for interpolating the density and the force between the particle positions and the grid in the two RAMSES-based codes. The blue lines show that the ΛCDM results obtained with ISIS and ECOSMOG are in very good agreement (<1 per cent error for all scales and times shown) if both codes use the same interpolation scheme, in this case CIC. This shows that the modifications made to RAMSES to develop ECOSMOG and ISIS do not introduce any systematics in the way the codes work for GR.[6] On the other hand, compared to the ECOSMOG run with TSC, the power in ISIS is higher by ≈3 per cent, (7 per cent) for $z = 0$, ($z = 1$), for $k \approx 7\,h\,\mathrm{Mpc}^{-1}$. This is because the CIC interpolation distributes the mass of each particle into fewer grid cells, which results in higher peaks in the density field, compared to TSC. We note that the size of the differences between ISIS and ECOSMOG to MG-GADGET are comparable to the differences induced by different interpolation schemes.

5.2.2 f(R)

The $f(R)$ model was simulated with ECOSMOG, MG-GADGET and ISIS. In all codes, the relaxation of the scalar field equation was performed on an AMR grid. The results are shown in the middle and right-hand panels of Fig. 2 for the F5 and F6 $f(R)$ models, respectively. Fig. 3 shows the relative difference to ΛCDM in F5 (left) and F6 (right) for $z = 0, 1, 2$. This depicts the known result that the modifications to gravity in this model boost structure formation on small scales and that these effects are stronger in the F5 than in the F6 model. It is perhaps also interesting to note that, for the F5 model at $z = 0$, the relative difference to ΛCDM does not flatten out on scales $k \lesssim 0.1\,h\,\mathrm{Mpc}^{-1}$, which are scales on which the growth is scale independent in ΛCDM. This shows that in modified gravity, the naive expectation (inspired from ΛCDM) for the scales on which the growth of structure is scale independent can be misleading (Hellwing et al. 2013b).

The differences observed in the right-hand panels of Fig. 2 are similar in shape and size to those in the left-hand panel for ΛCDM, which suggests that the calculation of the fifth force is consistent in between the three codes. This is confirmed by the result depicted in Fig. 3, which shows the good agreement between the three codes for all scales and times shown.[7] In particular, at $z = 0$ ($z = 2$), all codes agree to within 1 per cent for scales $k < 7\,h\,\mathrm{Mpc}^{-1}$ ($k \lesssim 5\,h\,\mathrm{Mpc}^{-1}$). From this, we can conclude that any differences between these three modified gravity codes for $f(R)$ are driven almost exclusively by the differences in their main codes (in this case RAMSES and GADGET), and not by the extra modules that solve for the effects of the fifth force. This is a very reassuring result.

---

[6] We note that the versions of the ISIS and ECOSMOG used in this paper are not built on the exact same release of RAMSES, which explains why their ΛCDM results are not 'exactly' the same.

[7] Note that MG-GADGET agrees well with the two RAMSES-based codes on small scales. This shows that any errors arising from summation errors in the tree algorithm in GADGET do not translate into discrepant power-spectrum results.
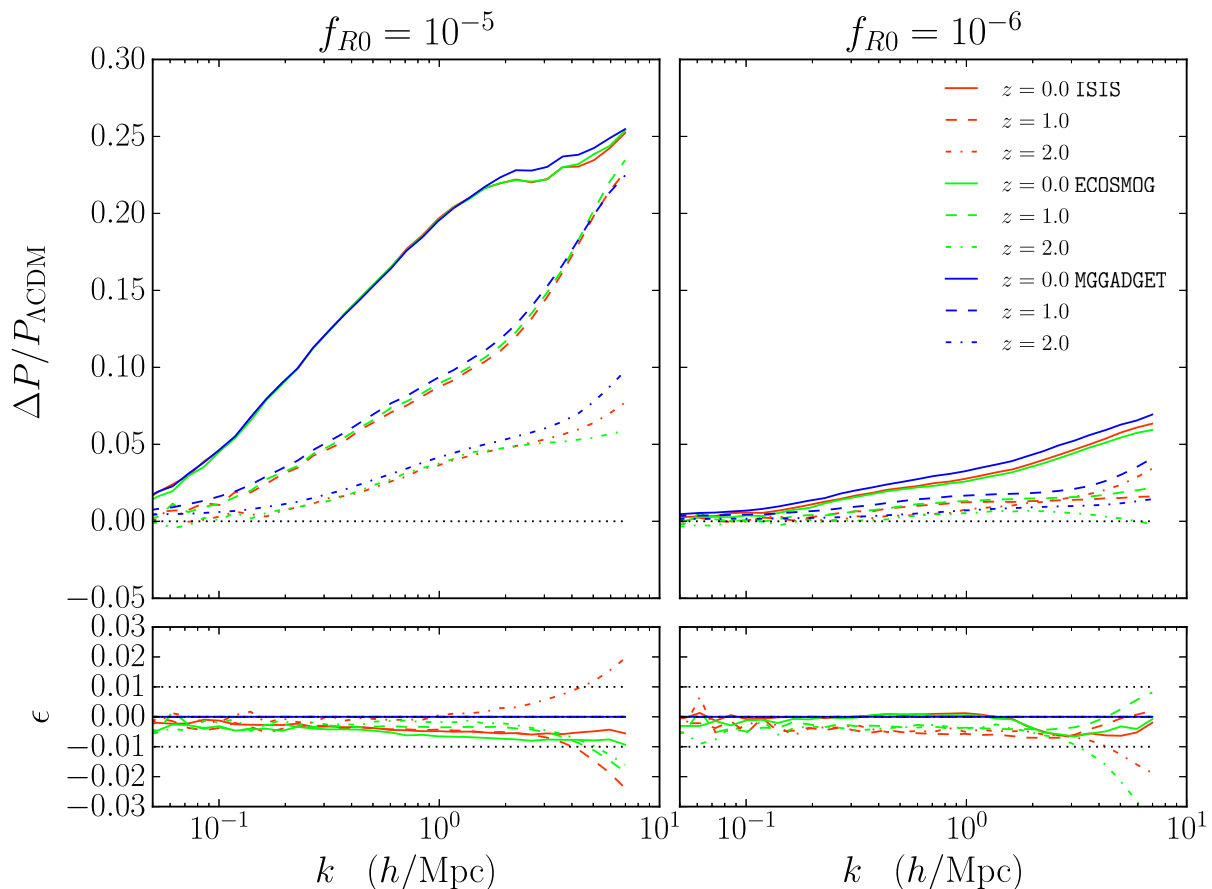
Figure 3. Fractional difference of the matter power spectrum with respect to ΛCDM from the simulations of the F5 (left) and F6 (right) models performed with the ECOSMOG (TSC), MG-GADGET and ISIS codes, as labelled. In the lower panel insets, $\epsilon = (P/P_{\Lambda\text{CDM}})_{\text{code}}/(P/P_{\Lambda\text{CDM}})_{\text{ref}} - 1$, with MG-GADGET being the reference code. At $z = 0$, the codes are all accurate to within 1 per cent on all scales shown.

5.2.3 DGP

The simulations of the DGP model were performed with the DGPM and ECOSMOG codes. The latter was run both with refinements and with a fixed grid to better compare with DGPM, which is fixed grid only. The top panel of Fig. 4 shows the ratio of the ΛCDM power spectrum of the DGPM to ECOSMOG simulations without refinements for $z = 0$ and $z = 1$. The lower panels of Fig. 4 show the relative difference to ΛCDM measured in the simulations of the $r_cH_0 = 5$ (left) and $r_cH_0 = 1$ (right) DGP models. We recover the known result that, in the DGP model, the amplitude of the power spectrum is boosted by a scale-independent factor on scales $k \lesssim 0.1 \, h \, \text{Mpc}^{-1}$. On mildly non-linear scales, $0.1 \, h \, \text{Mpc}^{-1} \lesssim k \lesssim 1 \, h \, \text{Mpc}^{-1}$, the boost in the power spectrum is stronger than on linear scales due to mode-coupling. However, on non-linear scales, $k \gtrsim 1 \, h \, \text{Mpc}^{-1}$ (halo size scales), the suppression effects of the Vainshtein screening mechanism are dominant, which effectively reduces the impact of the fifth force on the power spectrum (e.g. Schmidt, Hu & Lima 2010).

Fig. 4 shows that the three codes agree very well (up to 1 per cent) on scales $k \lesssim 1 \, h \, \text{Mpc}^{-1}$. For $k \gtrsim 1 \, h \, \text{Mpc}^{-1}$, however, the power in the DGPM simulations is higher than in ECOSMOG. This is due to the different interpolation schemes used in the codes. In particular, in DGPM, the CIC interpolation yields a density field with higher peaks than the density field in ECOSMOG, which is smoother because of the use of the TSC scheme. This is similar to the ECOSMOG and ISIS

results in the left-hand panel of Fig. 2 (blue and pink lines). The lower panels of Fig. 4 also show the ECOSMOG result with refinements (blue). For the $r_cH_0 = 5$ model the three codes are, overall, in good agreement for all redshifts and scales shown (<1 per cent for $k \lesssim 5 \, h \, \text{Mpc}^{-1}$). However, the modifications to gravity in the $r_cH_0 = 5$ model are weaker than in the $r_cH_0 = 1$ case, and as a result, it is easier to interpret the code results for the $r_cH_0 = 1$ model. For this case, the three codes agree very well for $k \lesssim 1 \, h \, \text{Mpc}^{-1}$. Note also that the ECOSMOG results with refinements agree with its results for fixed grid on these large scales. For $k \gtrsim 1 \, h \, \text{Mpc}^{-1}$, DGPM is also in good agreement with the results from ECOSMOG for fixed grid. Recall that the two codes solve the DGP scalar field equation in substantially different ways (cf. Section 4.2.2), so this is a non-trivial test. On these small scales, the agreement of the fixed-grid codes with the ECOSMOG code with refinements gets worse, but this is expected due to the gain in resolution in the latter. It is also interesting to note that, at $z = 0$ and for $k \gtrsim 4 \, h \, \text{Mpc}^{-1}$, the enhancement in the power is smaller in the ECOSMOG simulations with refinements compared to the fixed-grid cases. The explanation here is that the AMR nature of the grid allows it to resolve better the higher density peaks that exist on these smaller scales. This results in the code capturing better the suppression effects of the screening, and hence, the boost in the power relative to ΛCDM becomes less pronounced. This is more pronounced at $z = 0$ compared to $z = 1$ because at earlier times the density field is less evolved, hence the screening efficiency is also weaker.
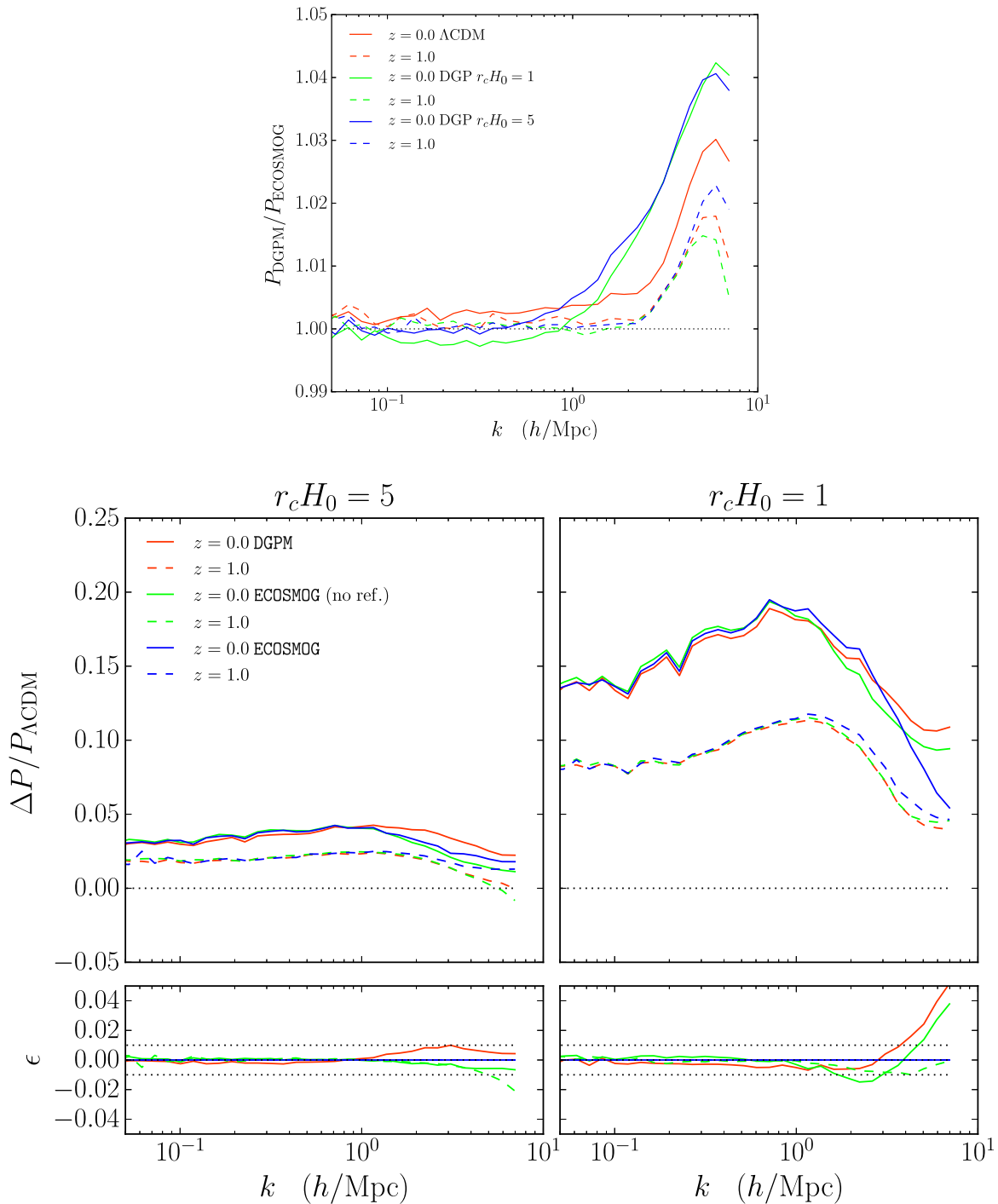
Figure 4. The top panel shows the comparison of the matter power-spectrum results of the DGPM and ECOSMOG (fixed grid) simulations of the ΛCDM, $r_cH_0 = 5$ and $r_cH_0 = 1$ DGP models, as labelled. The lower left and lower right panels show the fractional difference with respect to ΛCDM of the two codes for the $r_cH_0 = 5$ and $r_cH_0 = 1$ DGP models, respectively. The lower panels show the ECOSMOG results both for fixed and refined grid simulations, as labelled. In the lower panel insets, $\epsilon = (P/P_{\Lambda CDM})_{\rm code}/(P/P_{\Lambda CDM})_{\rm ref} - 1$, with ECOSMOG (refined grid) being the reference code.

In summary, we conclude that the two available *N*-body implementations of the Vainshtein screening agree well in the non-refining case, with the differences from the refined case appearing fully consistent with being due to the higher resolution of the latter. In the future, it would be desirable to also test an independent implementation of Vainshtein screening with refinements.

5.2.4 Symmetron

The left-hand panel of Fig. 5 shows the power-spectrum results for the Symmetron model, which were obtained with the ISIS and ISIS-NONSTATIC code, both run without refinements. The figure shows that the impact of the time-derivative terms in the equation of the Symmetron model, equation (52), is below the 0.5 per cent level
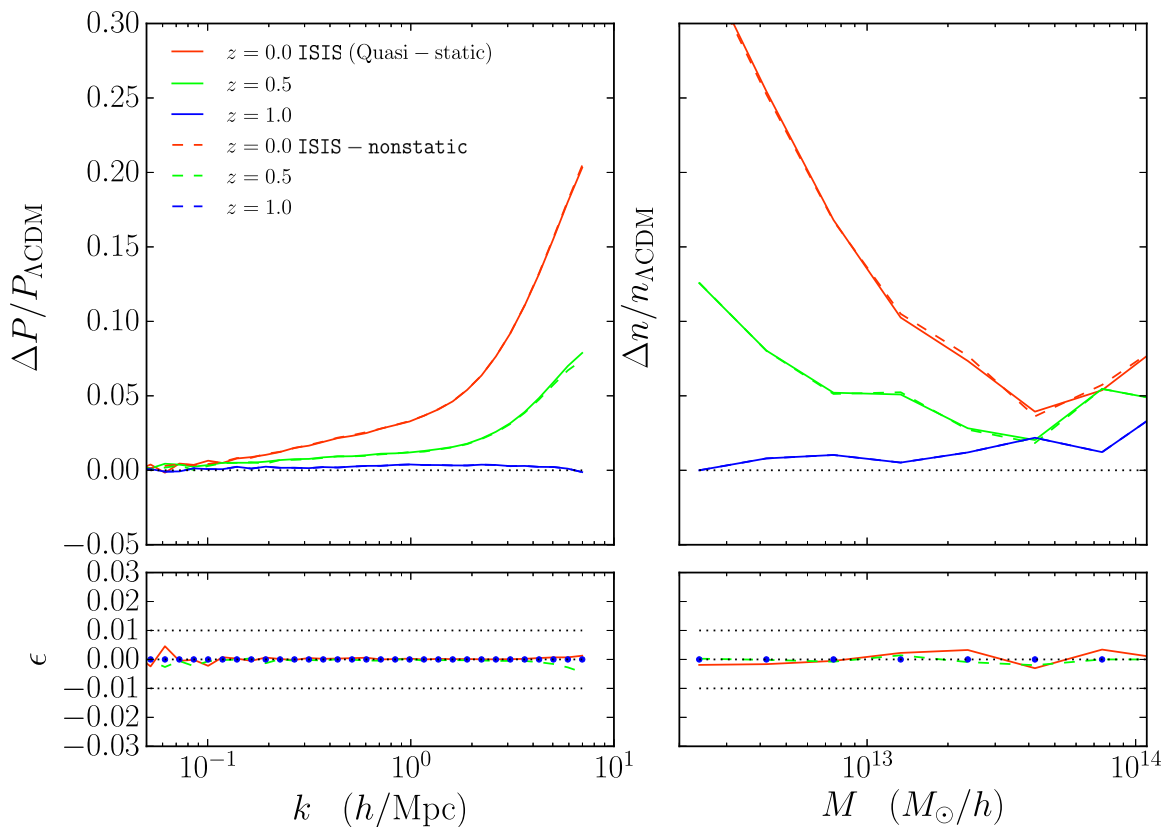
Figure 5. Comparison of the matter power-spectrum (left) and halo mass function (right) results of the Symmetron model simulations performed by the ISIS and ISIS-NONSTATIC codes. The lower panels shows the error induced by applying the quasi-static approximation, $\epsilon = P_{\text{Quasi-static}}/P_{\text{Full}} - 1$, whereas the upper panels shows the fractional difference relative to ΛCDM, as labelled. In all panels, the error induced by employing the quasi-static limit lies comfortably below 1 per cent for all the times and scales shown.

for all times and scales shown. Moreover, there seems to be no trend with scale. Hence, we can conclude that, in what concerns measurements of the non-linear matter power spectrum from *N*-body simulations of the Symmetron model, the use of the quasi-static limit has virtually no impact on the results.

This result is not unexpected since the calculation of the matter power spectrum is dominated by high-density regions (haloes, if one thinks about it in the framework of the halo model), where the time derivatives are indeed expected to be negligible relative to the spatial ones. Consequently, it may be of interest to investigate whether the quasi-static assumption remains also a good approximation for observables which are more sensitive to lower density regions. Such an investigation is not explored in this study.

It would also have been good to have a comparison with MG-GADGET and ECOSMOG for the Symmetron model but we leave this to future work. A brief comparison of $P(k)$ for the (quasi-static) Symmetron model and the codes ISIS, ECOSMOG and MLAPM can be found in Llinares et al. (2014).

5.3 Velocity divergence spectra

We have measured the power spectrum of the velocity divergence field defined as $P_{\theta\theta}(k) \equiv \langle\theta_k^2\rangle$, where $\theta(x) = H_0^{-1}\nabla \cdot v(x)$, with v being the peculiar velocity field. In the linear regime, θ is related to the matter density contrast as $\theta \propto -\delta f$, where $f = \mathrm{dln}\delta/\mathrm{dln}a$ is the linear growth rate. We show only results for the divergence of the velocity field, but note that on small scales, where non-linear

processes become important, the vorticity (rotational component of $v(x)$) is non-negligible and hence the whole velocity field cannot be described solely by θ.

To measure $P_{\theta\theta}(k)$, we constructed a volume-weighted velocity field (Bernardeau & van de Weygaert 1996) with the DTFE method implemented in the publicly available code of Cautun & van de Weygaert (2011). We refer the reader to Li et al. (2013c) for more details about our method to compute the velocity divergence field from the *N*-body particle positions and velocities. Next, we discuss our results for the $f(R)$ and DGP simulations. We have also measured $P_{\theta\theta}$ for the Symmetron simulations of the ISIS and ISIS-NONSTATIC codes, but since there are virtually no differences between the full and quasi-static results, we refrain from showing them.

5.3.1 $f(R)$

Fig. 6 shows the fractional difference of the velocity divergence power spectrum with respect to ΛCDM in the F5 (left) and F6 (right) models. The enhancement in the amplitude of $P_{\theta\theta}$ in $f(R)$ relative to ΛCDM is noticeably larger than that seen for the matter power spectrum (see also Jennings et al. 2012; Li et al. 2013b,c; Hellwig et al. 2014). In particular, for the F5 (F6) model at $z = 0$ and $k \approx 3\,h\,\mathrm{Mpc}^{-1}$, the amplitude of $P_{\theta\theta}$ is enhanced by ≈ 50 per cent (≈ 20 per cent), while the boost in the amplitude of $P(k)$ is kept at 20–25 per cent (≈ 5 per cent) only. The velocity field is more sensitive than the density field to the modifications to gravity because it
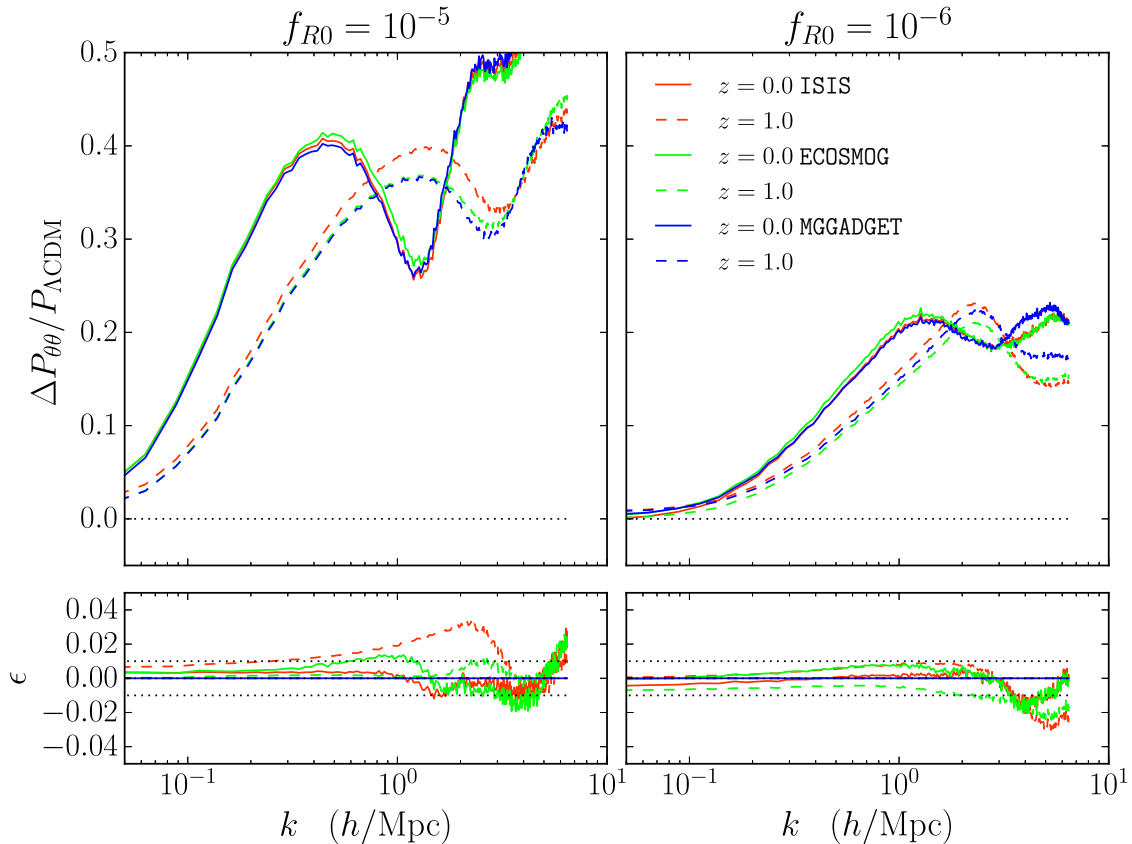
Figure 6. Fractional difference of the velocity divergence power spectrum with respect to ΛCDM from the simulations of the F5 (left) and F6 (right) models performed with the ECOSMOG (CIC), MG-GADGET and ISIS codes, as labelled. In the lower panel insets, $\epsilon = (P/P_{\Lambda\text{CDM}})_{\text{code}}/(P/P_{\Lambda\text{CDM}})_{\text{ref}} - 1$, with MG-GADGET being the reference code.

starts to be affected at earlier times, and the effects get accumulated throughout the history of structure growth.

As in the case of the matter power spectrum, the agreement between ECOSMOG, MG-GADGET and ISIS is notable. In particular, for both F5 and F6 at $z = 0$, the three codes agree up to ≈ 1 per cent down to $k \sim 3\, h\,\text{Mpc}^{-1}$, and for higher k-values the difference never exceeds 2 per cent. The case of the ISIS code for F5 at $z = 1$ is an exception to this very good agreement, for which the difference with the other two codes is at the 2–4 per cent level for $k \sim 0.3$–$3\, h\,\text{Mpc}^{-1}$. We have checked that at $z = 2$ the agreement between the three codes is at the 1–2 per cent level, which suggests that the larger disagreement at $z = 1$ could be due to a transient effect related, for instance, to differences in the time integration.[8] We leave a more thorough investigation of this difference for future work.

5.3.2 DGP

Fig. 7 shows the fractional difference of the velocity divergence power spectrum with respect to ΛCDM in the $r_{\text{c}}H_0 = 5$ (left) and $r_{\text{c}}H_0 = 1$ (right) DGP models. The agreement between DGPM and ECOSMOG is very good, with any differences in $r_{\text{c}}H_0 = 5$ predictions being below ≈ 1 per cent for all times and scales shown. For the $r_{\text{c}}H_0 = 1$ model, the agreement between the codes worsens, but the

difference is always below the 2 per cent level. Similarly to the case of the $f(R)$ model, we also note that the modifications to gravity in the DGP model affect the amplitude of $P_{\theta\theta}$ more than they affect the amplitude of $P(k)$.

In Fig. 7, it is interesting to note that on small scales ($k \gtrsim 2$–$3\, h\,\text{Mpc}^{-1}$), the difference between the fixed (red and green) and refined grid (blue) results is smaller than that seen in Fig. 4 for the matter power spectrum. Given the gain in resolution when ECOSMOG is run with refinements, one does not expect the results to fully agree with fixed-grid simulations which cannot resolve small-scale structures, and as a result, the agreement depicted in Fig. 7 may seem surprising. We do not perform any detailed investigations of this result, but simply note that the density field used to compute $P(k)$ is mass weighted, whereas the density field used to compute $P_{\theta\theta}$ is volume weighted. This, together with the suppressed contribution of virial velocities to the velocity divergence, may help explain why the use of adaptively refined grids does not have a critical impact on the resulting $P_{\theta\theta}$. For completeness, we further note that, as found in Falck, Koyama & Zhao (2015), peculiar velocities on small scales are also less affected by the Vainshtein mechanism, compared to the effects of the Chameleon mechanism.

5.4 Halo mass function

The halo mass function, $n(M)$, defined as the number density of dark matter haloes with mass M, is an important statistic that is particularly sensitive to modifications to gravity. We used a modified

---

[8] For example, slight differences in the AMR structure and velocity field in the ECOSMOG and ISIS simulations can result in different time step sizes (determined by the same criteria as in standard RAMSES).
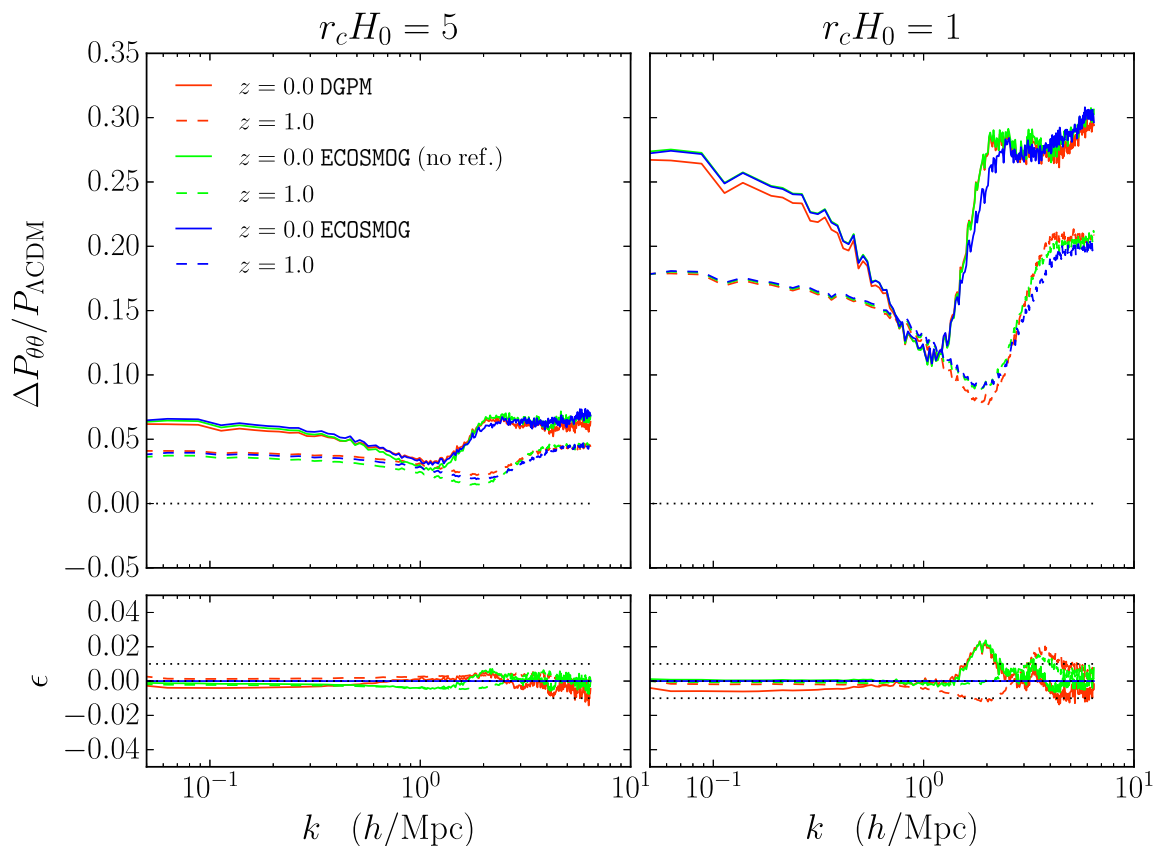
Figure 7. Fractional difference of the velocity divergence power spectrum with respect to ΛCDM from the simulations of the $r_c H_0 = 5$ (left) and $r_c H_0 = 1$ (right) DGP models performed with the DGPM and ECOSMOG codes. The two sets of ECOSMOG results correspond to the results from simulations run with fixed and refined grids, as labelled. In the lower panel insets, $\epsilon = (P/P_{\Lambda\text{CDM}})_{\text{code}}/(P/P_{\Lambda\text{CDM}})_{\text{ref}} - 1$, with ECOSMOG (refined grid) being the reference code.

version of the spherical overdensity AMIGA'S HALO FINDER (AHF) code (Gill, Knebe & Gibson 2004; Knollmann & Knebe 2009) to identify dark matter haloes and calculate their profiles. For this, simulation outputs from all codes were written in the standard GADGET2 format, but with new data blocks added, which contain the components of standard gravity and the fifth force as well as the Newtonian potential and the scalar field at particle positions. We outputted quantities at particle positions rather than leaf cells of the AMR grids or trees because, unlike the leaf cells, the particle IDs are the same in all simulations, making comparisons more straightforward. Note that this means that the scalar field and forces in underdense regions were not very well sampled, which however should not be a serious issue given that we are mostly interested in haloes.

The major modifications to AHF were threefold: (i) new routines to read the above data, which has the same format as the default GADGET2 data such as particle coordinates and velocities; (ii) new routines to compute the force and scalar field profiles in haloes, by averaging over their values at all particle positions in a given spherical shell (the radial binning scheme for this was the same as in the default AHF code) and (iii) the routine in AHF which does the removal of unbound particles was also modified so that the code determined whether a particle was bound or not by comparing its velocity with the total gravitational potential instead of the standard Newtonian potential. Note that if (iii) is not properly done, then the mass function tends to be lower because more particles are considered as too fast to be bound. Li & Zhao (2010) studied the effect of taking account the fifth force in the halo unbinding process

for certain Chameleon models using *N*-body simulations and found a noticeable difference in the resulting mass functions (see also Hellwing, Knollmann & Knebe 2010; Hellwing et al. 2013a).

We used AHF with $\Delta_{\text{vir}} = 200$ so that $M_{\text{AHF}} = M_{200c}$. Next, we discuss our mass function results for the $f(R)$, DGP and Symmetron simulations.

5.4.1 f(R)

Figs 8 and 9 show the mass function results of the ECOSMOG, ISIS and MG-GADGET simulations for $f(R)$. As first shown quantitatively in Schmidt et al. (2009), $f(R)$ models predict an enhancement in the abundance of haloes relative to ΛCDM. The enhancement is more pronounced in the F5 model because the Chameleon screening is less efficient. This is particularly noticeable at the high-mass end for which, in the F6 model, the number density of haloes is almost the same as in ΛCDM. The differences in the mass dependence of $\Delta n/n_{\Lambda\text{CDM}}$ for different $f(R)$ model parameters and redshifts illustrates the complex interplay between the mass and time dependence of the Chameleon screening mechanism (see e.g. Lombriser, Koyama & Li 2014; Shi et al. 2015; Gronke, Mota & Winther 2015b; Gronke et al. 2015a; Gronke, Llinares & Mota 2014; Winther, Mota & Li 2012, for studies of halo properties in $f(R)$).

Fig. 8 shows the ratio of the ECOSMOG and ISIS results to those of MG-GADGET for the ΛCDM (left-hand panel), F5 (middle panel) and F6 (right-hand panel) models. The three codes show varying levels of agreement (between 2 and 10 per cent) throughout the
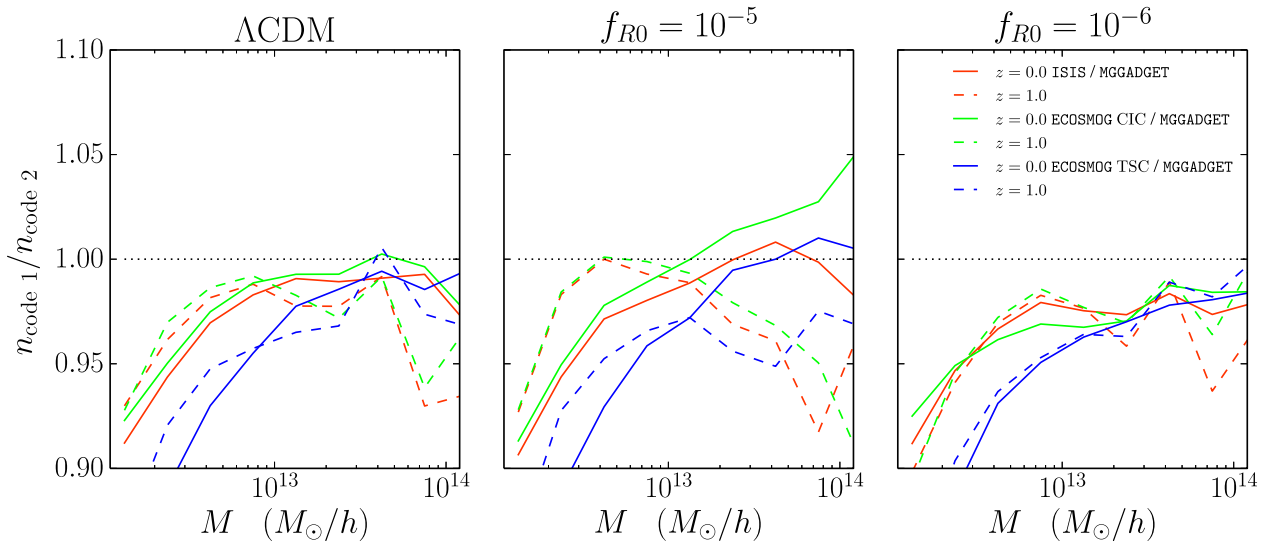
Figure 8. Comparison of the halo mass function results of the ECOSMOG, MG-GADGET and ISIS codes for the ΛCDM (left), F5 (middle) and F6 (right) models, as labelled. The two sets of ECOSMOG results correspond to the results from simulations using the CIC and TSC density assignment, as labelled.
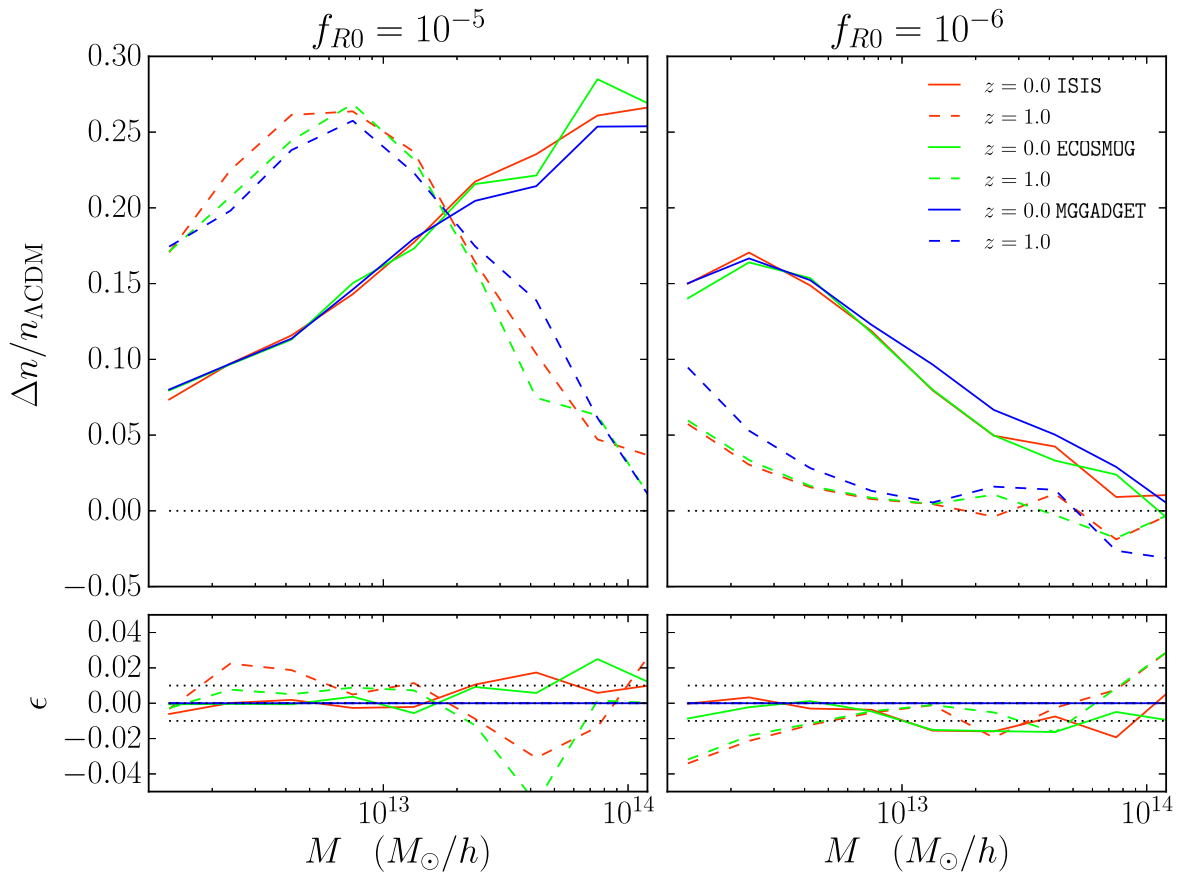

Figure 9. Fractional difference of the halo mass function with respect to ΛCDM from the simulations of the F5 (left) and F6 (right) models performed with the ECOSMOG (TSC), MG-GADGET and ISIS codes, as labelled. In the lower panel insets, $\epsilon = (n/n_{\Lambda\text{CDM}})_{\text{code}}/(n/n_{\Lambda\text{CDM}})_{\text{ref}} - 1$, with MG-GADGET being the reference code.

mass range probed by our simulations and for the two redshifts shown. In particular, at $z = 0$ and intermediate mass scales, $M \sim 10^{13}\,\text{M}_\odot\,h^{-1}$, ECOSMOG and ISIS agree with MG-GADGET at $\lesssim 4$ per cent, but the agreement worsens to 5–10 per cent for smaller mass scales.

At the high-mass end, $M \sim 10^{14}\,\text{M}_\odot\,h^{-1}$, the finite box size limits us to only a few halo samples, which is why the high-mass end is noisy (as can be checked by the scatter between different mass bins). Overall, the trend is for the two RAMSES-based codes to underpredict

the abundance of smaller mass haloes, compared to MG-GADGET. This discrepancy can be linked to the way the base codes RAMSES and P-GADGET3 compute the force on small scales (see discussion in Section 5.2). Also, there is a marked improvement in the agreement between ECOSMOG and ISIS when the two codes are run with the same density assignment scheme (CIC in this case).

The amplitude and shape of the curves in Fig. 8 is similar for ΛCDM and the two $f(R)$ models, which indicates that differences between the modified gravity codes are mostly driven by differences in the default codes. Indeed, this is again confirmed by the result of Fig. 9 which shows the fractional difference in the $f(R)$ mass functions relative to ΛCDM. One notes that the three codes agree very well, especially at $z = 0$, echoing the results seen in the previous two sections for the matter and velocity divergence power spectra.

5.4.2 DGP

The top panel of Fig. 10 shows the ratio of the mass function results obtained with the DGPM code to those obtained with ECOSMOG (both with and without refinements) for the simulations of the ΛCDM and $r_c H_0 = 5$ and $r_c H_0 = 1$ DGP models. For the three models, there is a systematic trend for DGPM to produce more massive haloes than ECOSMOG, even when ECOSMOG is run without refinements like DGPM. This result can be linked to the different density assignments of the two codes (CIC for DGPM versus TSC for ECOSMOG). The lower panels of Fig. 10 show that the agreement between the two codes improves when one looks at the fractional difference of the two DGP models to ΛCDM. For the case of the $r_c H_0 = 5$ model, although there are still visible differences between the results of the two codes, these remain of the same order as the bin-to-bin scatter. The agreement worsens slightly for the $r_c H_0 = 1$ model. Overall, both DGPM and ECOSMOG are in good agreement in their predictions for $\Delta n / n_{\Lambda CDM}$, although to a lesser extent than the agreement for the matter and velocity power spectra seen in the previous sections (Figs 4 and 7).

5.4.3 Symmetron

The right-hand panel of Fig. 5 measures the impact of the quasi-static limit on the mass function of the Symmetron model, as predicted by the ISIS and ISIS-NONSTATIC codes (both run without refinements). As seen in the case of the mass power spectrum (upper panels), relaxing the quasi-static approximation has no appreciable effect on halo abundances: differences are $\lesssim 0.5$ per cent and have no clear dependence on mass.

5.5 Halo profiles

Finally, we turn our attention to the code results for the radial profiles of the density, velocity dispersion, force and scalar field around dark matter haloes. For this, we used the $z = 0$ AHF halo catalogues of each simulation and binned them in mass according to: $[5 \times 10^{12}, 1 \times 10^{13}]$, $[1 \times 10^{13}, 5 \times 10^{13}]$, $[5 \times 10^{13}, 1 \times 10^{14}]$ and $[1 \times 10^{14}, 5 \times 10^{14}]$ M$_\odot$ h^{-1}. For each mass bin, we scaled the AHF haloes by their virial radii (determined by the AHF code) and stacked them to compute average profiles of the different quantities. We take the variance of this average as the error bars. The density, scalar field, and force profiles are calculated using all particles around a given AHF halo centre, which includes particles that lie beyond the AHF halo. On the other hand, the velocity dispersion profiles are

calculated using only particles defined to be part of the AHF halo, thus they only extend out to the virial radius.

As before, we discuss our results for the halo profiles in turn for the $f(R)$, DGP and Symmetron models.

5.5.1 $f(R)$

We plot the profiles of the scalar field in Fig. 11, of the force modulus in Fig. 12, and of the density and velocity dispersion in Fig. 13 for the haloes found in the F5 and F6 ECOSMOG, MG-GADGET and ISIS simulations. The ECOSMOG results in these figures correspond to the runs performed with the CIC interpolation scheme (as in ISIS). For MG-GADGET, the force profiles shown are those calculated by interpolating the gradient of the scalar field from the grid to the particle positions instead of the effective density method (recall the discussion about fig. 1 in Section 4.2.1). The gradient method captures more accurately the suppression effects of the screening in the inner regions of the haloes.

Overall, the ISIS and ECOSMOG codes agree very well, with any deviations typically lying within the error bars in the profiles depicted in Figs 11–13. This is reassuring but not very surprising, considering that they are both based on RAMSES and are run with the same settings. It is therefore more interesting to compare ISIS and ECOSMOG with MG-GADGET, for which some differences exist. For instance, although at large radii there is good agreement between the scalar field profiles obtained by the three codes, in the inner regions of the haloes there is not. This is particularly noticeable in the F6 model at $r/r_{vir} \lesssim 1$ (right-hand panels of Fig. 11), for which MG-GADGET overpredicts the values of f_R compared to ECOSMOG and ISIS. In the F5 model, the discrepancies soften considerably, especially for the low-mass haloes. These differences in the f_R profiles naturally translate into differences in the amplitude of the fifth force on small radial scales, as seen in the lower four panels of Fig. 12. However, the lower panels of Fig. 12 show that the discrepancies between MG-GADGET and the two RAMSES-based codes are only appreciable when the fifth force is a small fraction ($\lesssim 0.1$) of the total force (due to screening). This means that, although the codes may disagree on their exact predictions for the amplitude of the modifications to gravity, they only do so in regimes where the fifth force is not very important anyway. This is confirmed by the fact that the density and velocity dispersion profiles shown in Fig. 13 agree very well (there are differences of order 5 per cent, which we note are likely to come from differences in the base codes.)

At large radii ($r/r_{vir} \gtrsim 1$), MG-GADGET overpredicts the amplitude of the Newtonian force compared to ECOSMOG and ISIS. Here, we stress that what we average in a given halo mass bin is the force modulus and not any directional component of the force (e.g. radial). This is why the force profiles do not keep decaying towards large radii but instead level off due to the matter distribution that surrounds the haloes.[9] This can explain the mismatch in the Newtonian force at large radii because the matter distribution around haloes in GADGET and RAMSES simulations is not exactly the same, and the base code algorithms that compute the Newtonian force are also different. What is important here is that, at these large radii, the three codes agree very well in their fifth force predictions, which are the corrections to normal gravity we are interested in testing in this paper.

---

[9] If one would average the radial component of the force for a large number of haloes, then the contribution from the surrounding structure would cancel out.
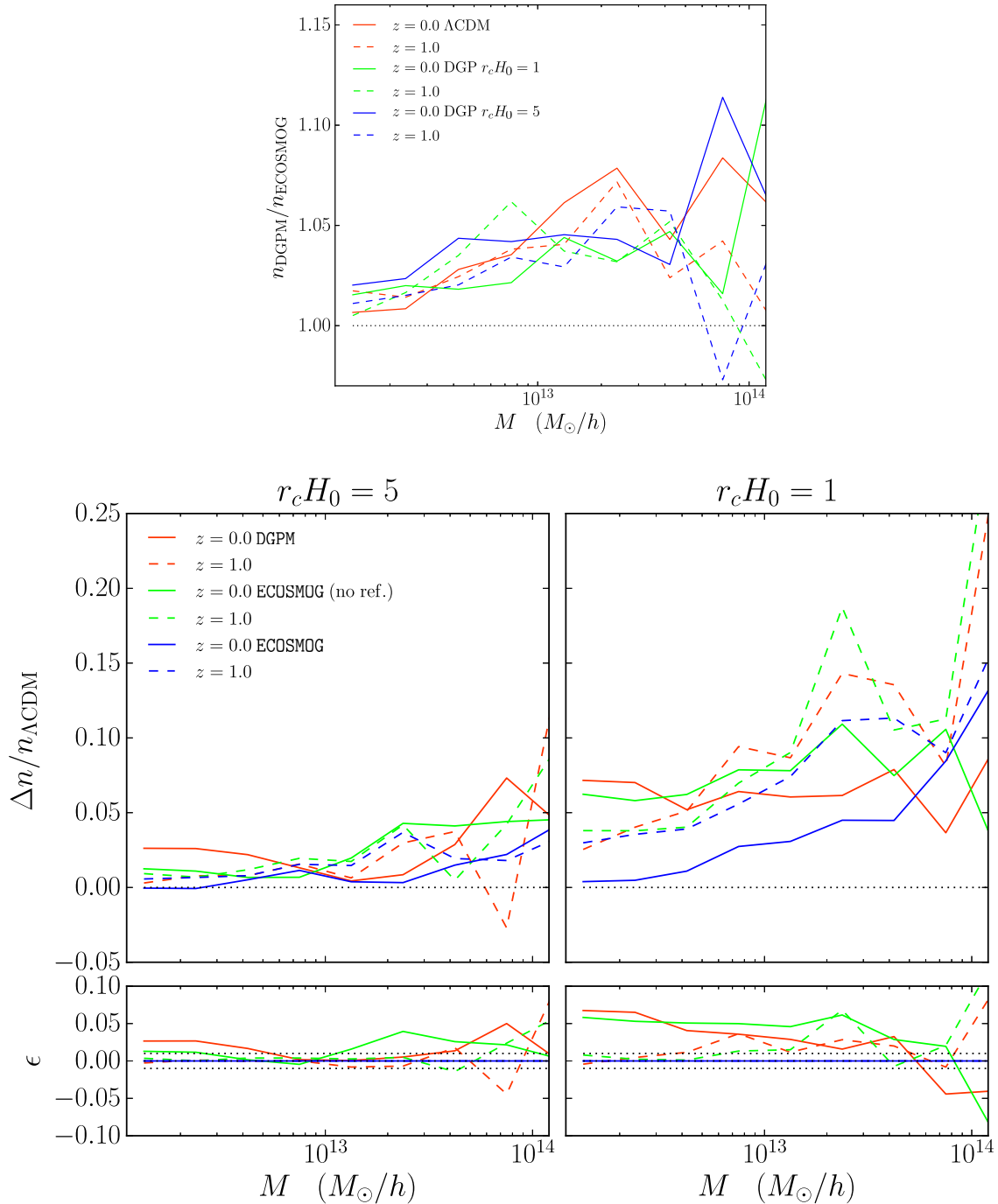
Figure 10. The top panel shows the comparison of the halo mass function results of the DGPM and ECOSMOG (fixed grid) simulations of the ΛCDM, $r_c H_0 = 5$ and $r_c H_0 = 1$ DGP models, as labelled. The lower left and lower right panels show the fractional difference with respect to ΛCDM of the two codes for the $r_c H_0 = 5$ and $r_c H_0 = 1$ DGP models, respectively. The lower panels show the ECOSMOG results both for fixed and refined grid simulations, as labelled. In the lower panel insets, $\epsilon = (n/n_{\Lambda CDM})_{code}/(n/n_{\Lambda CDM})_{ref} - 1$, with ECOSMOG (refined grid) being the reference code.

5.5.2 DGP

Figs 14 and 15 show the same as Figs 12 and 13, but for the DGP simulations performed with the DGPM and ECOSMOG (with and without refinements) codes. The absolute value of the scalar field in the DGP model is irrelevant as the equations of the model contain only its derivatives. For this reason, we do not show the scalar field profiles and prefer to plot the gradient of the field (which, up to a factor of 1/2, is the fifth force as seen in equation 15).

The Newtonian force profiles of the two codes are in very good agreement when ECOSMOG is run without refinements (like DGPM). There are marked differences in the solutions of the two codes for the size of the fifth force in the inner regions of the haloes, but since the amplitude of the fifth force is small there anyway, the difference does not translate into the density and velocity dispersion profiles (as seen in Fig. 13). However, when analysing these results, it is important to bear in mind that the grid size of the non-refined
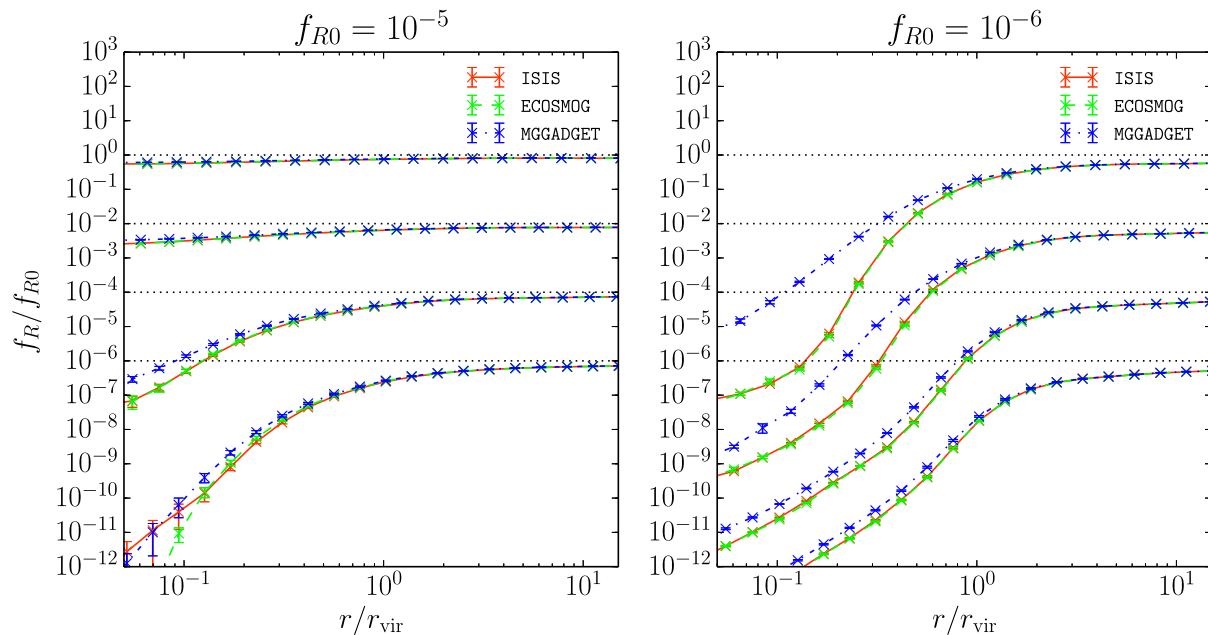
Figure 11. Radial profiles of the f_R scalar field in dark matter haloes found in the simulations of the ECOSMOG (CIC), MG-GADGET and ISIS codes for the F5 (left) and F6 (right) models. The result is shown for the following four halo mass bins: $M \in [1 \times 10^{14}, 5 \times 10^{14}]$, $M \in [5 \times 10^{13}, 1 \times 10^{14}]$, $M \in [1 \times 10^{13}, 5 \times 10^{13}]$ and $M \in [5 \times 10^{12}, 1 \times 10^{13}]$ $M_\odot\, h^{-1}$ (from bottom to top). For clarity, the profiles for each mass bin are displaced vertically, with the four horizontal lines (also displaced vertically) indicating $f_R/f_{R0} = 1$ of each mass bin.

simulations ($\Delta r \simeq 0.5\,h^{-1}$ Mpc) is half of the typical halo size scales of $\approx 1\,h^{-1}$ Mpc. As a result, one should not attempt to draw any physically meaningful conclusions from the results depicted by the red and green lines. We showed these lines simply to illustrate that the DGPM and ECOSMOG (non-refined) codes agree in their total force profiles, even though their solutions may not be accurate.

When ECOSMOG is run with refinements on the grid, the code is able to better resolve the matter distribution in and around the haloes. The top panels of Fig. 15 show that the density profiles of the non-refined simulations only agree with those of the refined simulation for $r/r_{\rm vir} \gtrsim$ 5–10. This provides a measure for the radial scales below which one should not trust the non-refined simulations. It is also interesting to note that the ratio of the fifth to Newtonian force does not depend on halo mass, as seen in the lower panels of Fig. 14. This illustrates that the efficiency of the Vainshtein mechanism in the DGP model is independent of the mass of the haloes (Schmidt 2010; Falck et al. 2014, 2015), which is different from what is seen in the lower panels of Fig. 12 for the $f(R)$ models.

5.5.3 Symmetron

Fig. 16 shows the radial profiles of the scalar field and of the fifth to Newtonian force ratio obtained from the ISIS and ISIS-NONSTATIC simulations of the Symmetron model. The scalar field in the ISIS-NONSTATIC simulations oscillates very rapidly with time. For this case, the profiles we show represent the mean value averaged over several oscillations close to $z = 0$. We note also that since these simulations were performed on a fixed grid, they suffer from the same resolution problems as the non-refined DGP runs. This prevents the simulations from fully capturing a number of effects such as the efficiency of the screening. Nevertheless, for the sake of determining the impact of the quasi-static limit these issues can be ignored. The result of Fig. 16 reinforces the conclusions drawn previously that

relaxing the quasi-static limit has little impact on the simulations of the Symmetron model.

6 SUMMARY AND CONCLUSIONS

N-body simulations of modified gravity play a key role in cosmological tests of gravity using LSS observations. In this work, we have performed an extensive comparison of the simulation results of $f(R)$, DGP and Symmetron gravity using five modified gravity *N*-body codes, which were the DGPM, ECOSMOG, MG-GADGET, ISIS and ISIS-NONSTATIC codes. In the models we simulated, the gravitational law is modified due to the presence of a fifth force mediated by a scalar field. The algorithms in these codes differ from those for standard gravity by having extra modules that iteratively relax the equation of the scalar field on a grid/mesh to determine the fifth force. The ISIS-NONSTATIC code is a version of the ISIS code that goes beyond the quasi-static approximation that is often employed in modified gravity studies. We used this code to test the validity of this assumption in the case of the Symmetron model.

The modified gravity routines included in the modified gravity codes are typically installed in existing and well tested *N*-body codes for GR (such as RAMSES or P-GADGET3). Since these main codes can show some level of disagreement in their results for standard ΛCDM, then these differences would naturally propagate into the modified gravity results. To overcome this, in this paper we have run also simulations of standard ΛCDM, which were used as a reference to measure the effects of the modifications to gravity. Hence, our main concern in this paper was to compare the code predictions for the fractional difference with respect to ΛCDM of a given quantity, and not so much its absolute values.

All our simulations of the different models and codes start from the same set of initial conditions, which allows a direct comparison between the results. We analysed the code results for the power spectrum of the matter density fluctuations and peculiar velocity
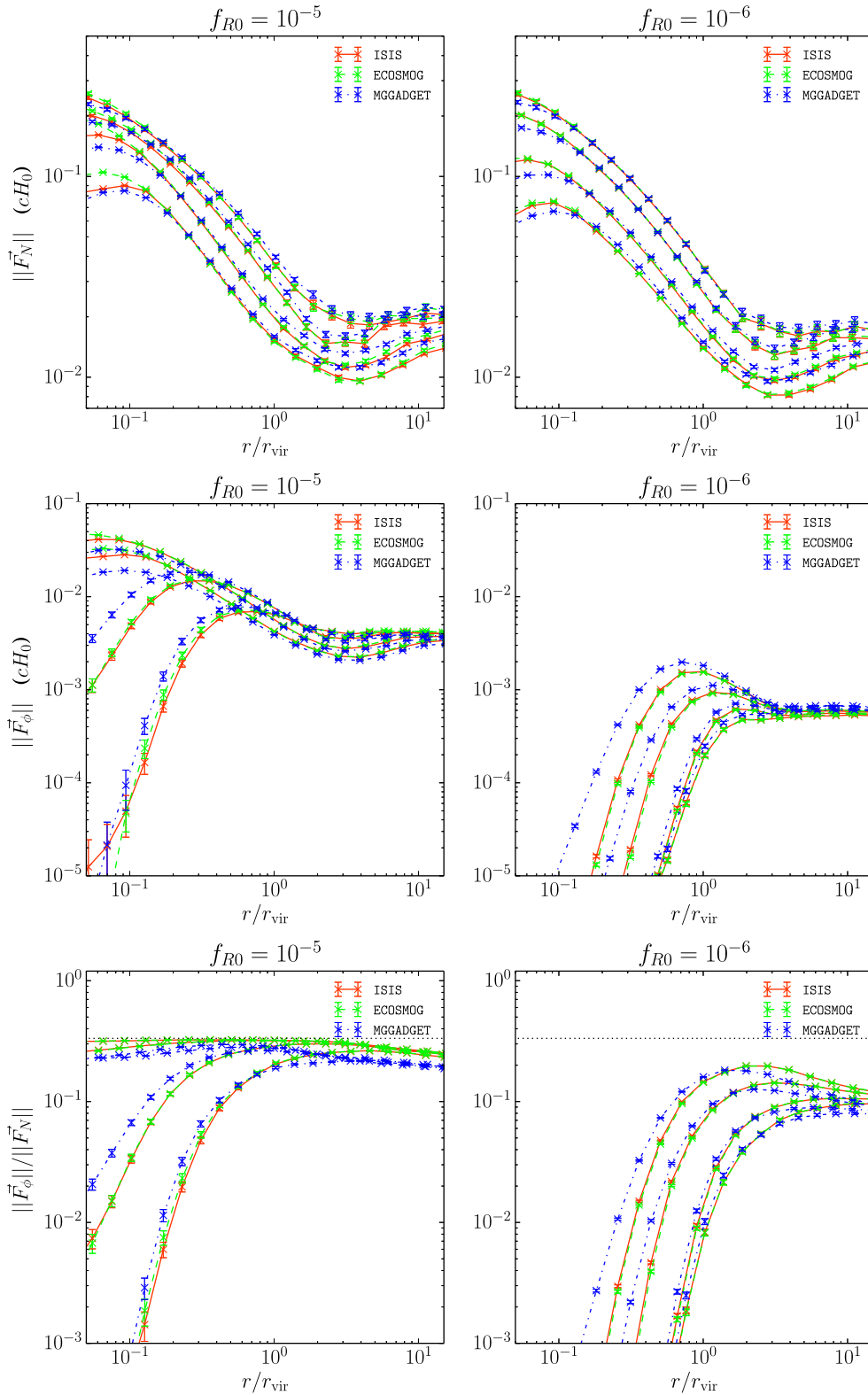
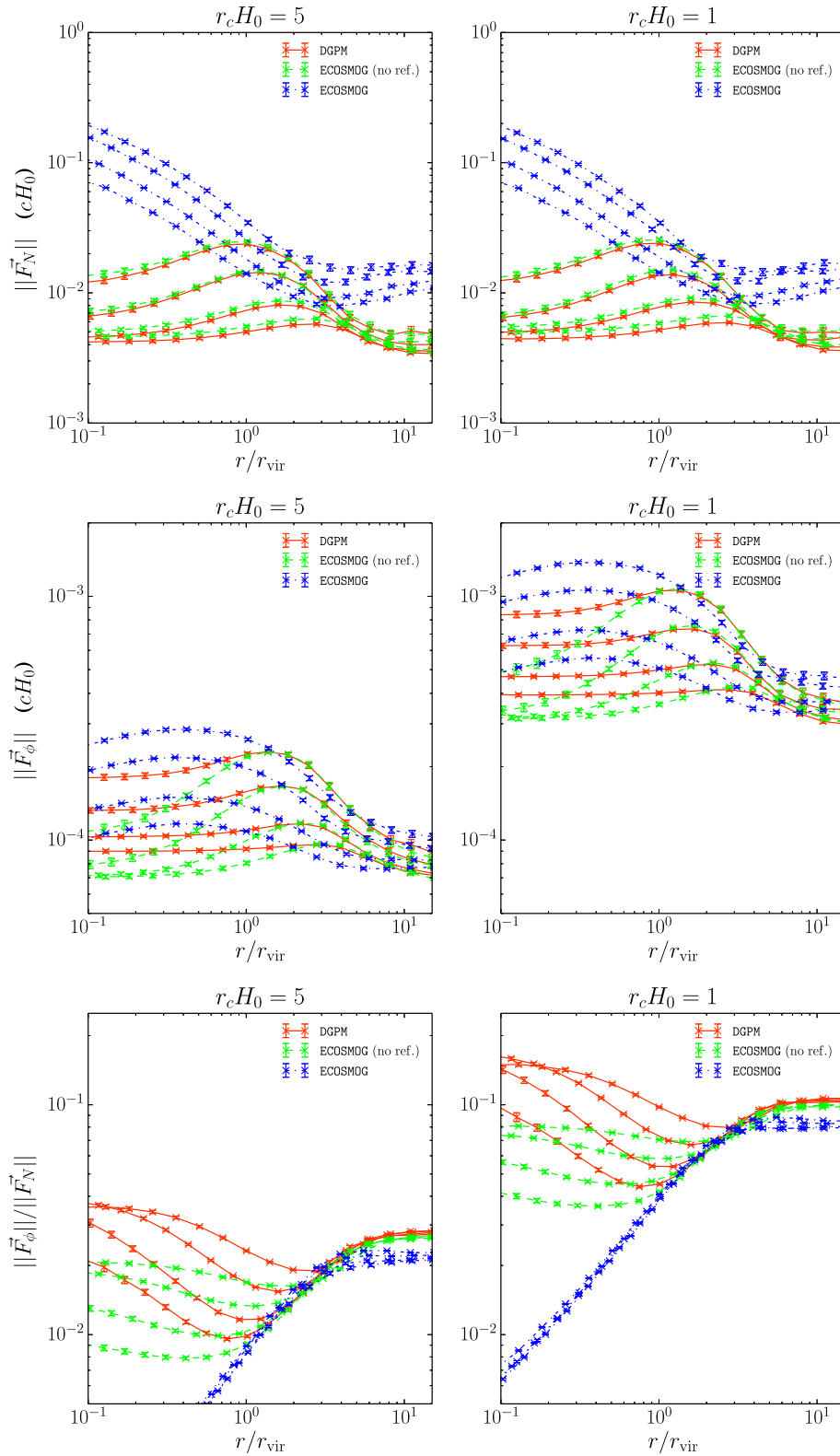**Figure 12.** Radial profiles of the Newtonian force (upper), fifth force (middle) and fifth to Newtonian force ratio (bottom) for haloes in the F5 (left) and F6 (right) simulations, performed with the ECOSMOG (CIC), MG-GADGET and ISIS codes, as labelled. The result is shown by splitting haloes into the same mass bins used in Fig. 11. In this case, however, the results for each bin are not displaced vertically. In the lower panels, the horizontal lines show $F_\phi/F_N = 1/3$, which is the expected value in the absence of screening. When determining the force profiles in each mass bin, what is averaged is the force moduli of the haloes, and not its radial component.
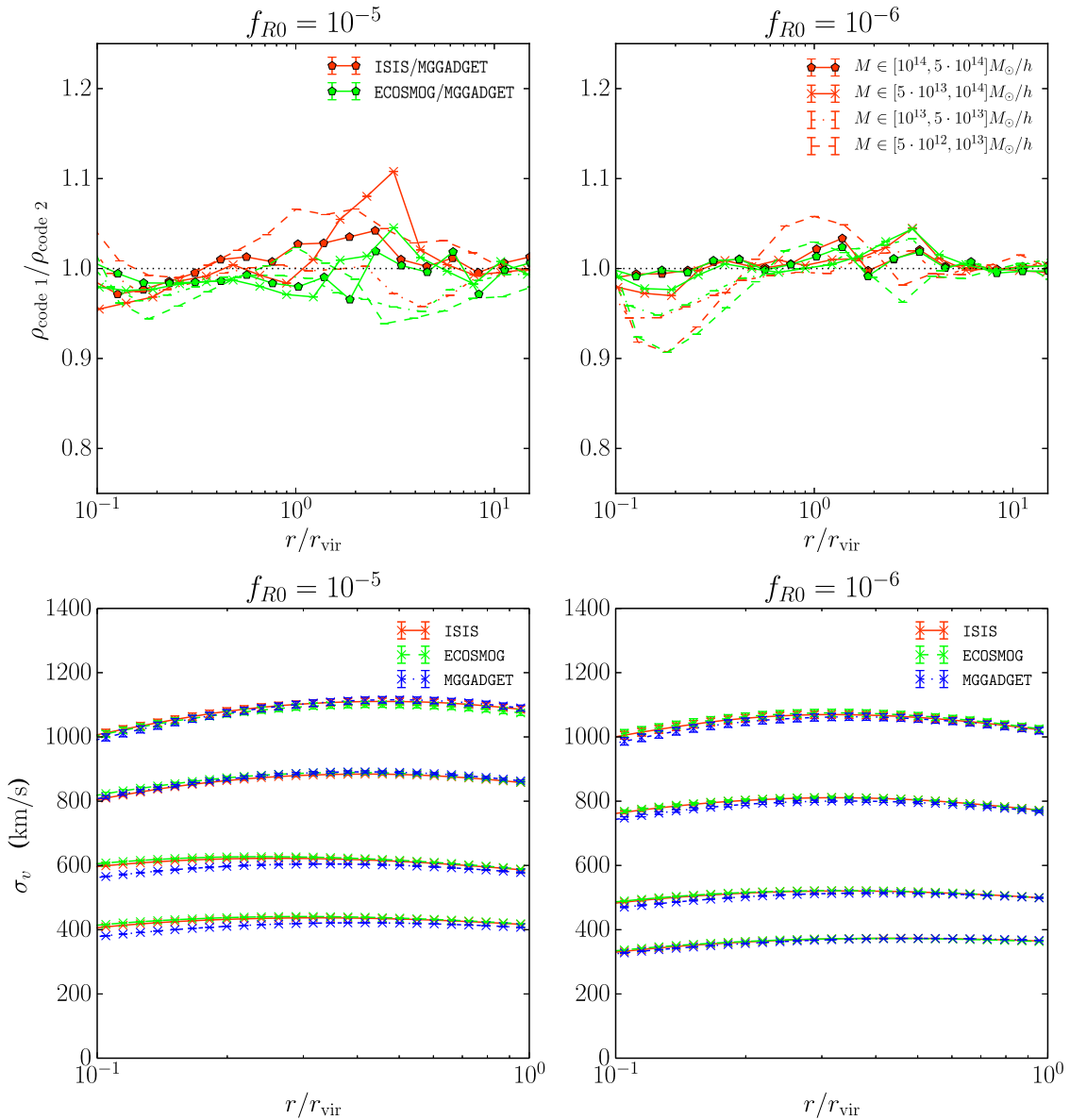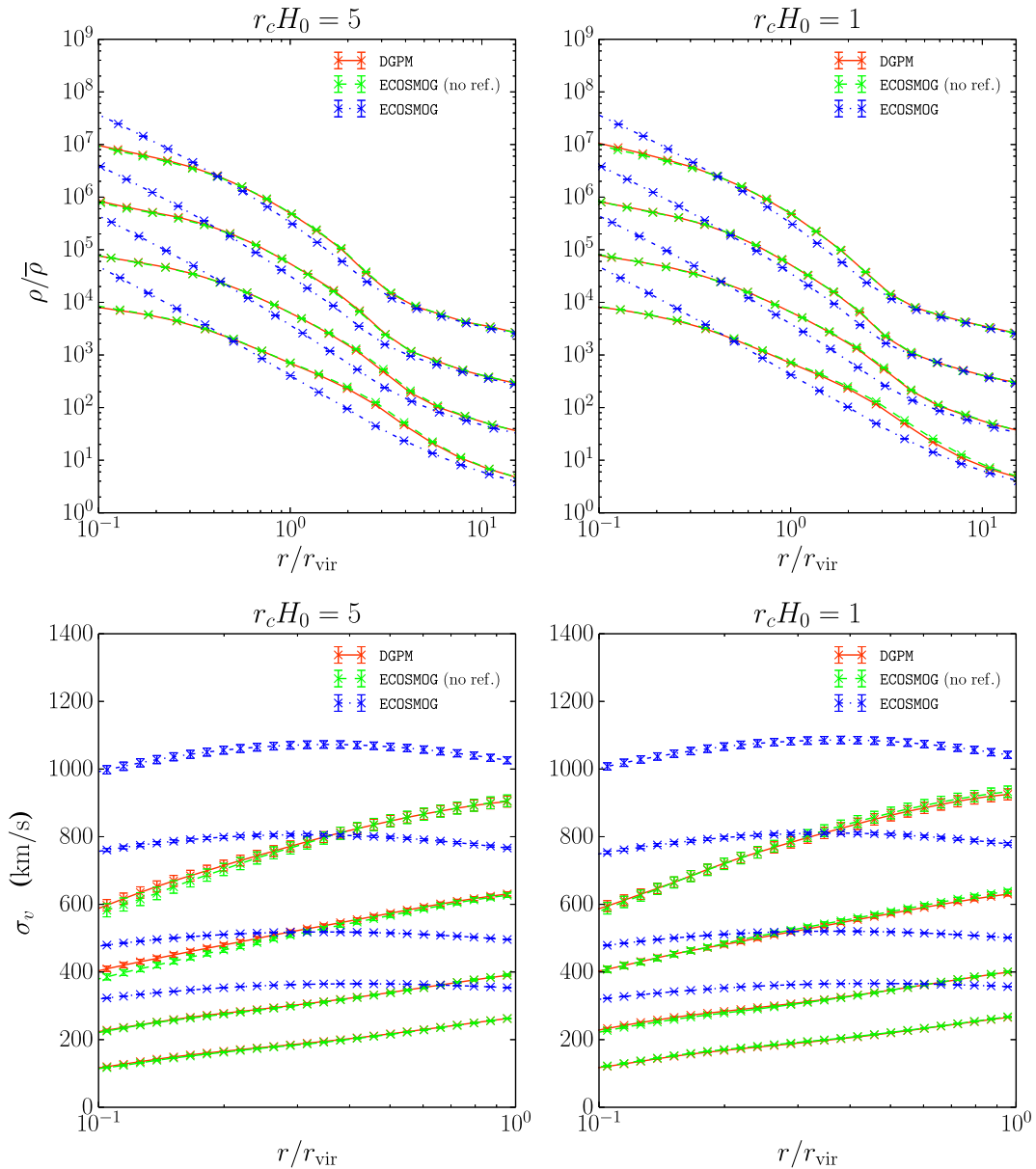
Figure 13. Radial profiles of the density (upper) and velocity dispersion (bottom) for haloes in the F5 (left) and F6 (right) simulations, performed with the ECOSMOG (CIC), MG-GADGET and ISIS codes, as labelled. The result is shown by splitting the haloes into the same mass bins used in Figs 11 and 12. Note that in the lower panels the profile is only shown up to $r/r_{\rm vir} = 1$.

divergence. We have also compared results for the abundances of dark matter haloes and for their density, velocity dispersion and force profiles.

We have generally found agreement at the few-per cent level in the properties of the matter density and velocity fields. This means that modified gravity simulations satisfy the accuracy requirements of currently planned LSS surveys, provided that the absolute calibration of GR predictions is of comparable accuracy.

In what follows, we recap the main results of this comparison project in more detail.

(1) Matter power spectrum. Given its immediate relation to galaxy redshift and lensing observables, the matter power spectrum $P(k)$ is one of the most important observables for tests of gravity. For ΛCDM, we found that the modified gravity codes (run with the routines for modified gravity switched off) agree up to 1 per cent for $k \lesssim 1\,h\,{\rm Mpc}^{-1}$, but start differing on smaller scales ($\sim$5 per cent at $k \sim 5\,h\,{\rm Mpc}^{-1}$) due to different density and force assignments schemes and intrinsic algorithmic differences in the force calculation in AMR (for ECOSMOG and ISIS) and TreePM (for MG-GADGET) codes (cf. Fig. 2).

For the $f(R)$ simulations, which were performed with the ECOSMOG, MG-GADGET and ISIS codes, we find that any differences in $P(k)$ are driven almost exclusively by the differences in the base codes (RAM-SES and P-GADGET3 respectively). In terms of the relative difference to ΛCDM, all code results for $f(R)$ agree to better than 1 per cent for $k \lesssim 7\,h\,{\rm Mpc}^{-1}$ (cf. Fig. 3).

While ECOSMOG and ISIS are based on the same GR code and use very similar algorithms, MG-GADGET is sufficiently different to make this a non-trivial consistency test.

Figure 14. Radial profiles of the Newtonian force (upper), fifth force (middle) and fifth to Newtonian force ratio (bottom) for haloes in the $r_cH_0 = 5$ (left) and $r_cH_0 = 1$ (right) simulations, performed with the DGPM and ECOSMOG codes. The ECOSMOG results are shown for both the fixed and refined grid simulations, as labelled. The result is shown by splitting haloes into the same mass bins as used in Fig. 12. When determining the force profiles, what is averaged is the force moduli, and not its radial component. Note also that for all mass scales, the AMR nature of the grid plays a key role in the measured force profiles.

Figure 15. Radial profiles of the density (upper) and velocity dispersion (bottom) for haloes in the $r_cH_0 = 5$ (left) and $r_cH_0 = 1$ (right) simulations, performed with the DGPM and ECOSMOG codes. The ECOSMOG results are shown for both the fixed and refined grid simulations, as labelled. The result is shown by splitting the haloes into the same mass bins used in Fig. 14. For clarity, the result for the different mass bins has been displaced vertically in the density panels. In these, the differences between the two codes for fixed grid are kept below ≈5 per cent for all mass bins and scales shown. Note that in the lower panels the profile is only shown up to $r/r_{vir} = 1$.

The simulations of the DGP model were performed with the DGPM and ECOSMOG codes. The former code does not have an adaptive mesh, but ECOSMOG can be run on both a fixed and refined mesh. For the fixed-grid case, the two codes are in very good agreement in their predictions for the relative difference to ΛCDM (≲1 per cent for $k \lesssim 7\,h\,\mathrm{Mpc}^{-1}$; cf. Fig. 4). This is a non-trivial test since the DGP scalar field solvers in DGPM and ECOSMOG are substantially different. The fixed grid simulations start to differ from the refined grid simulations on small scales, but this is expected since the latter is able to resolve small scales much better.

For the test of the validity of the quasi-static limit in the Symmetron model, we have seen that the results from ISIS and ISIS-NONSTATIC are nearly indistinguishable (cf. Fig. 5). We conclude that

the impact of adding the time-derivative terms to the Symmetron field equation of motion is negligible (<0.5 per cent on all scales and redshifts shown). We note, however, that in the current implementation of the time derivatives in the ISIS-NONSTATIC code, the particles do not feel the details of the rapid oscillations of the scalar field, due to the difference in the particle and scalar field time steps (see Llinares & Mota 2014, for more details). In the future, it would be of interest to clarify whether using the same time steps for particles and the scalar field has an impact on the results presented here.

(2) Velocity power spectrum. In terms of the velocity divergence power spectrum, $P_{\theta\theta}$, we have found that ECOSMOG, MG-GADGET and ISIS are again in very good agreement in their predictions for the
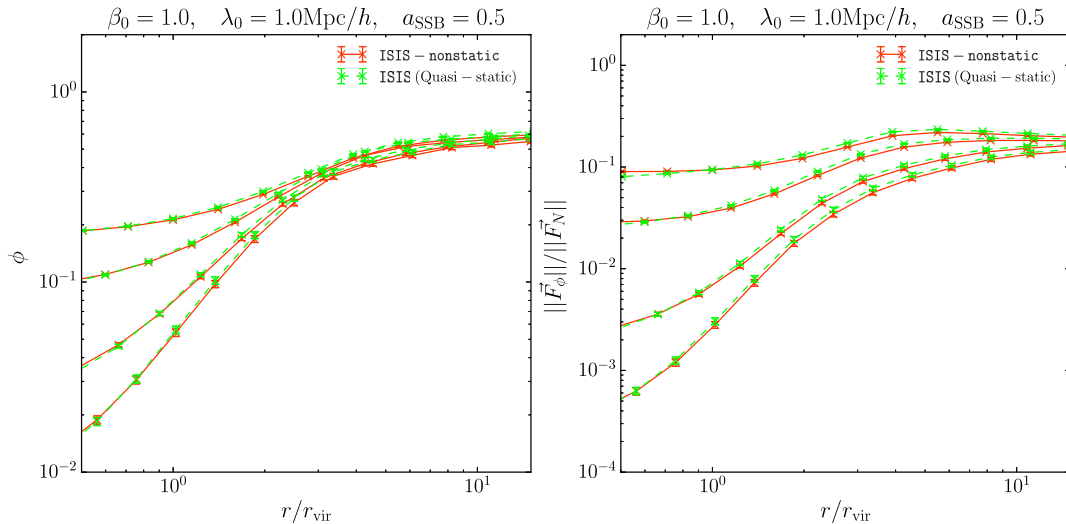
Figure 16. Radial profiles of the scalar field (left) and of the fifth to Newtonian force ratio (right) for haloes in the Symmetron model simulations, performed with the ISIS and ISIS-NONSTATIC codes. The result is shown by splitting the haloes into the same mass bins used in the figures of the $f(R)$ and DGP models. As in Fig. 5, the quasi-static limit remains an extremely good approximation.

fractional difference with respect to ΛCDM in $f(R)$ models. At $z = 0$, the three codes agree to better than 1 per cent for $k \lesssim 3\,h\,\mathrm{Mpc}^{-1}$, for both the F5 and F6 models (cf. Fig. 6). For the DGP simulations, the DGPM and ECOSMOG codes are also in very good agreement, with their predictions differing by $\lesssim 2$ per cent for both models simulated and for all times and scales shown (cf. Fig. 7). Interestingly, we have also seen that the $P_{\theta\theta}$ results of the DGP simulations on small scales are not critically affected by the use of a fixed or refined grid. For brevity, we did not show the impact of the quasi-static limit on $P_{\theta\theta}$ in the Symmetron model, but we have checked that it is negligible (just like for $P(k)$).

These results are encouraging as the precise modelling of cosmic velocity fields is a crucial ingredient in connecting the theoretically predicted clustering statistics in real space with the observed galaxy redshift space power spectrum.

(3) Halo mass function. The good agreement outlined above for the matter and peculiar velocity divergence power spectrum holds also for the halo mass function. Given the relatively small simulation volume, the accuracy of the mass function comparison is limited by cosmic variance. However, we are still able to conclude that the codes agree to a satisfactory level. In particular, for $f(R)$, the code predictions for $\Delta n/n_{\Lambda\mathrm{CDM}}$ agree up to ≈ 4 per cent for all mass scales probed by our simulation box (cf. Fig. 9). For the DGP simulations the agreement is at the 5–10 per cent level (cf. Fig. 10). Like for $P(k)$, the inclusion of the time-derivative terms in the Symmetron model equations leads to negligible differences only ($\lesssim 0.5$ per cent).

(4) Halo profiles. Understanding dark matter halo profiles in modified gravity is crucial to devise tests of gravity using galaxy clusters (Lam et al. 2012; Terukina & Yamamoto 2012; Lam et al. 2013; Zu et al. 2014; Lombriser et al. 2012; Wilcox et al. 2015; Barreira et al. 2015; Terukina et al. 2015). For the $f(R)$ simulations, although there are significant differences in the fifth force profiles of the RAMSES-based codes and MG-GADGET in the inner regions of the haloes (cf. Fig. 12), these do not translate into differences in the resulting density and velocity divergence profiles because they only appear in regions where the force modification is highly suppressed by Chameleon screening (cf. Fig. 13).

Similarly, the fifth force halo profiles of the DGPM and ECOSMOG (fixed grid) DGP simulations also differ, but only in the inner regions of the haloes, where the fifth force is already weak (cf. Fig. 14). We note, however, that although it is reassuring that the two codes agree in their halo density and velocity dispersion profiles (which is a cross-check of the validity of the algorithms), the resolution of the fixed grid prevents us from trusting their physical results on halo size scales. Indeed, the DGP simulations run with ECOSMOG (refined grid) show very different results, due to the gain in resolution (cf. Fig. 15).

The halo profiles in the Symmetron simulations performed with the ISIS and ISIS-NONSTATIC codes are nearly indistinguishable, which reinforces further the validity of the quasi-static limit (cf. Fig. 16).

Tests of gravity on large scales using galaxy power spectra, galaxy dynamics, cluster abundance, cluster profiles and so on are one of the main science drivers of many upcoming large surveys. Accurate simulations of non-linear structure formation in these models are therefore crucial to ensure robust theoretical predictions that can be compared with the observational data. In this paper, we have seen that the N-body codes that have been developed so far are in very good agreement for different models. This dedicated comparison project constitutes an important validity check of the different codes, which brings us one step closer to performing larger and more expensive modified gravity simulations to be used to prepare for several future observational efforts.

REFERENCES

Adelberger E. G., 2002, in Kostelecký V. A., ed., CPT and Lorentz Symmetry. World Scientific Press, USA, p. 9

Amendola L., Tsujikawa S., 2010, Dark Energy: Theory and Observations. Cambridge Univ. Press, Cambridge

Amendola L. et al., 2013, Living Rev. Relativ., 16, 6

Arnold C., Puchwein E., Springel V., 2014, MNRAS, 440, 833

Arnold C., Puchwein E., Springel V., 2015, MNRAS, 448, 2275

Babichev E., Deffayet C., Ziour R., 2009, Int. J. Mod. Phys. D, 18, 2147

Baldi M., Villaescusa-Navarro F., Viel M., Puchwein E., Springel V., Moscardini L., 2014, MNRAS, 440, 75

Barreira A., Li B., Hellwing W. A., Baugh C. M., Pascoli S., 2013a, J. Cosmol. Astropart. Phys., 010, 027

Barreira A., Li B., Baugh C. M., Pascoli S., 2013b, J. Cosmol. Astropart. Phys., 011, 056

Barreira A., Li B., Jennings E., Merten J., King L., Baugh C., Pascoli S., 2015, preprint (arXiv:1505.03468)

Bennett C. L. et al., 2013, ApJS, 208, 20

Bernardeau F., van de Weygaert R., 1996, MNRAS, 279, 693

Berti E. et al., 2015, preprint (arXiv:1501.07274)

Bertotti B., Iess L., Tortora P., 2003, Nature, 425, 374

Bose S., Hellwing W. A., Li B., 2015, J. Cosmol. Astropart. Phys., 002, 034

Brandt A., 1977, Math. Comp., 31, 333

Brax P., Valageas P., 2014, Phys. Rev. D, 90, 023507

Brax P., van de Bruck C., Davis A.-C., Shaw D. J., 2008, Phys. Rev. D, 78, 104021

Brax P., van de Bruck C., Davis A.-C., Shaw D., 2010, Phys. Rev. D, 82, 063519

Brax P., van de Bruck C., Davis A.-C., Li B., Shaw D. J., 2011a, Phys. Rev. D, 83, 104026

Brax P., van de Bruck C., Davis A.-C., Li B., Schmauch B., Shaw D. J., 2011b, Phys. Rev. D, 84, 123524

Brax P., Davis A.-C., Li B., Winther H. A., 2012a, Phys. Rev. D, 86, 044015

Brax P., Davis A.-C., Li B., Winther H. A., Zhao G.-B., 2012b, J. Cosmol. Astropart. Phys., 010, 002

Brax P., Davis A.-C., Li B., Winther H. A., Zhao G.-B., 2013, J. Cosmol. Astropart. Phys., 4, 029

Brito R., Terrana A., Johnson M. C., Cardoso V., 2014, Phys. Rev. D, 90, 124035

Burrage C., Khoury J., 2014, Phys. Rev. D, 90, 024001

Carroll S. M., Duvvuri V., Trodden M., Turner M. S., 2004, Phys. Rev. D, 70, 043528

Cautun M. C., van de Weygaert R., 2011, preprint (arXiv:1105.0370)

Chan K. C., Scoccimarro R., 2009, Phys. Rev. D, 80, 104005

Chuang C.-H. et al., 2015, MNRAS, 452, 686

Clifton T., Ferreira P. G., Padilla A., Skordis C., 2012, Phys. Rep., 513, 1

Colberg J. M. et al., 2008, MNRAS, 387, 933

Colombi S., Jaffe A., Novikov D., Pichon C., 2009, MNRAS, 393, 511

Crocce M., Pueblas S., Scoccimarro R., 2006, MNRAS, 373, 369

Davis A.-C., Li B., Mota D. F., Winther H. A., 2012, ApJ, 748, 61

Dvali G., Gabadadze G., Porrati M., 2000, Phys. Lett. B, 485, 208

Eisenstein D. J. et al., 2005, ApJ, 633, 560

Elahi P. J. et al., 2013, MNRAS, 433, 1537

Falck B., Koyama K., Zhao G.-b., Li B., 2014, J. Cosmol. Astropart. Phys., 007, 058

Falck B., Koyama K., Zhao G.-b., 2015, J. Cosmol. Astropart. Phys., 7, 049

Fang W., Wang S., Hu W., Haiman Z., Hui L., May M., 2008, Phys. Rev. D, 78, 103509

Gill S. P. D., Knebe A., Gibson B. K., 2004, MNRAS, 351, 399

Gronke M. B., Llinares C., Mota D. F., 2014, A&A, 562, A9

Gronke M., Llinares C., Mota D. F., Winther H. A., 2015a, MNRAS, 449, 2837

Gronke M., Mota D. F., Winther H. A., 2015b, preprint (arXiv:1505.07129)

Hagala R., Llinares C., Mota D. F., 2015, preprint (arXiv:1504.07142)

Hammami A., Mota D. F., 2015, preprint (arXiv:1505.06803)

Hammami A., Llinares C., Mota D. F., Winther H. A., 2015, MNRAS, 449, 3635

Hellwing W. A., Juszkiewicz R., 2009, Phys. Rev. D, 80, 083522

Hellwing W. A., Knollmann S. R., Knebe A., 2010, MNRAS, 408, L104

Hellwing W. A., Cautun M., Knebe A., Juszkiewicz R., Knollmann S., 2013a, J. Cosmol. Astropart. Phys., 010, 012

Hellwing W. A., Li B., Frenk C. S., Cole S., 2013b, MNRAS, 435, 2806

Hellwing W. A., Barreira A., Frenk C. S., Li B., Cole S., 2014, Phys. Rev. Lett., 112, 221102

Hinterbichler K., Khoury J., 2010, Phys. Rev. Lett., 104, 231301

Hinterbichler K., Khoury J., Levy A., Matas A., 2011, Phys. Rev. D, 84, 103521

Hoffmann K. et al., 2014, MNRAS, 442, 1197

Hu W., Sawicki I., 2007, Phys. Rev. D, 76, 064004

Jain B., Khoury J., 2010, Ann. Phys., 325, 1479

Jennings E., Baugh C. M., Li B., Zhao G.-B., Koyama K., 2012, MNRAS, 425, 2128

Joyce A., Jain B., Khoury J., Trodden M., 2015, Phys. Rep., 568, 1

Khoury J., Weltman A., 2004a, Phys. Rev. D, 69, 044026

Khoury J., Weltman A., 2004b, Phys. Rev. Lett, 93, 171104

Khoury J., Wyman M., 2009, Phys. Rev. D, 80, 064023

Kitching T. D., Taylor A. N., 2011, MNRAS, 416, 1717

Knebe A., Green A., Binney J., 2001, MNRAS, 325, 845

Knebe A., 2011, MNRAS, 415, 2293

Knebe A. et al., 2013a, MNRAS, 428, 2039

Knebe A. et al., 2013b, MNRAS, 435, 1618

Knollmann S. R., Knebe A., 2009, ApJS, 182, 608

Koivisto T. S., Mota D. F., Zumalacarregui M., 2012, Phys. Rev. Lett., 109, 241102

Koyama K., 2007, Classical Quant. Grav., 24, 231

Koyama K., 2015, preprint (arXiv:1504.04623)

Koyama K., Silva F. P., 2007, Phys. Rev. D, 75, 084040

Lam T. Y., Nishimichi T., Schmidt F., Takada M., 2012, Phys. Rev. Lett., 109, 051301

Lam T. Y., Schmidt F., Nishimichi T., Takada M., 2013, Phys. Rev. D, 88, 023012

Laureijs R. et al., 2011, preprint (arXiv:1110.3193)

Li B., Barrow J. D., 2011, Phys. Rev. D, 83, 024007

Li B., Zhao H., 2009, Phys. Rev. D, 80, 044027

Li B., Zhao H., 2010, Phys. Rev. D, 81, 104047

Li B., Mota D. F., Barrow J. D., 2011, ApJ, 728, 109

Li B., Zhao G.-B., Teyssier R., Koyama K., 2012, J. Cosmol. Astropart. Phys., 001, 051

Li B., Zhao G.-B., Koyama K., 2013a, J. Cosmol. Astropart. Phys., 005, 023

Li B., Barreira A., Baugh C. M., Hellwing W. A., Koyama K., Pascoli S., Zhao G.-B., 2013b, J. Cosmol. Astropart. Phys., 011, 012

Li B., Hellwing W. A., Koyama K., Zhao G.-B., Jennings E., Baugh C. M., 2013c, MNRAS, 428, 743

Llinares C., Mota D. F., 2013, Phys. Rev. Lett., 110, 161101

Llinares C., Mota D. F., 2014, Phys. Rev. D, 89, 084023

Llinares C., Pogosian L., 2014, Phys. Rev. D, 90, 124041

Llinares C., Mota D. F., Winther H. A., 2014, A&A, 562, A78

Lombriser L., Schmidt F., Baldauf T., Mandelbaum R., Seljak U., Smith R. E., 2012, Phys. Rev. D, 85, 102001

Lombriser L., Koyama K., Li B., 2014, J. Cosmol. Astropart. Phys., 003, 021

Lue A., Starkman G. D., 2004, Phys. Rev. D, 70, 101501

Luty M. A., Porrati M., Rattazzi R., 2003, J. High Energy Phys., 9, 29

Mota D. F., Shaw D. J., 2006, Phys. Rev. Lett., 97, 151102

Nicolis A., Rattazzi R., 2004, J. High Energy Phys., 6, 59

Nicolis A., Rattazzi R., Trincherini E., 2009, Phys. Rev. D, 79, 064036

Old L. et al., 2014, MNRAS, 441, 1513

Olive K. A., Pospelov M., 2008, Phys. Rev. D, 77, 043524

Onions J. et al., 2012, MNRAS, 423, 1200

Onions J. et al., 2013, MNRAS, 429, 2739

Oyaizu H., 2008, Phys. Rev. D, 78, 123523

Pearson J. A., 2014, Phys. Rev. D, 90, 125011

Pietroni M., 2005, Phys. Rev. D, 72, 043535

Planck Collaboration XIII 2015, preprint (arXiv:1502.01589)

Puchwein E., Baldi M., Springel V., 2013, MNRAS, 436, 348

Pujol A. et al., 2014, MNRAS, 438, 3205

Riess A. G. et al., 1998, AJ, 116, 1009

Sahni V., Shtanov Y., 2003, J. Cosmol. Astropart. Phys., 011, 014

Scannapieco C. et al., 2012, MNRAS, 423, 1726

Schaap W. E., van de Weygaert R., 2000, A&A, 363, L29

Schmidt F., 2009a, Phys. Rev. D, 80, 123003

Schmidt F., 2009b, Phys. Rev. D, 80, 043001

Schmidt F., 2010, Phys. Rev. D, 81, 103002

Schmidt F., Lima M., Oyaizu H., Hu W., 2009, Phys. Rev. D, 79, 083518

Schmidt F., Hu W., Lima M., 2010, Phys. Rev. D, 81, 063005

Schneider A. et al., 2015, preprint (arXiv:1503.05920)

Shi D., Li B., Han J., Gao L., Hellwing W. A., 2015, MNRAS, 452, 3179

Springel V., 2005, MNRAS, 364, 1105

Springel V., Hernquist L., 2002, MNRAS, 333, 649

Srisawat C. et al., 2013, MNRAS, 436, 150

Terukina A., Yamamoto K., 2012, Phys. Rev. D, 86, 103503

Terukina A., Yamamoto K., Okabe N., Matsushita K., Sasaki T., 2015, preprint (arXiv:1505.03692)

Teyssier R., 2002, A&A, 385, 337

Trottenberg U., Oosterlee C., Scholler A., 2000, Multigrid. Academic Press, New York

Vainshtein A. I., 1972, Phys. Lett. B, 39, 393

Viel M., Haehnelt M. G., Springel V., 2010, J. Cosmol. Astropart. Phys., 006, 015

Wesseling P., 1992, An Introduction to Multigrid Methods, 2nd edn. John Wiley and Sons Inc.

Wilcox H. et al., 2015, MNRAS, 452, 1171

Will C. M., 2014, Living Rev. Relativ., 17, 4

Williams J. G., Turyshev S. G., Boggs D. H., 2004, Phys. Rev. Lett., 93, 261101

Winther H. A., Ferreira P. G., 2015a, Phys. Rev. D, 91, 123507

Winther H. A., Ferreira P. G., 2015b, Phys. Rev. D, 92, 064005

Winther H. A., Mota D. F., Li B., 2012, ApJ, 756, 166

Zhao G.-B., Li B., Koyama K., 2011, Phys. Rev. D, 83, 044007

Zu Y., Weinberg D., Jennings E., Li B., Wyman M., 2014, MNRAS, 445, 1885

This paper has been typeset from a TEX/LATEX file prepared by the author.